UNIVERSITY OF CALIFORNIA, SAN DIEGO

Spontaneous coherence, kinetics and pattern formation in cold exciton gases in GaAs/AlGaAs Coupled Quantum Wells

A dissertation submitted in partial satisfaction of the
requirements for the degree
Doctor of Philosophy

in

Physics

by

Sen Yang

Committee in charge:

Professor Leonid V. Butov, Chair
Professor Yeshaiahu Fainman
Professor Lu J. Sham
Professor Sunil K. Sinha
Professor Charles W. Tu

2009

The dissertation of Sen Yang is approved, and it is acceptable in quality and form for publication on microfilm:

_____

_____

_____

_____

_____

Chair

University of California, San Diego

2009

DEDICATION

To my wife Zaoli and my parents

TABLE OF CONTENTS

LIST OF FIGURES

ACKNOWLEDGEMENTS

First of all, I would like to thank my advisor, Professor Butov, for taking me into his group and supporting me through these years. I'm very much obliged to his great ideas, profound knowledge in physics and guidance throughout the progress of the works. When I made mistakes and the progress is not as expected, he is patient with me. When we work too late in the lab, he always ask us to go home and take a rest. He cares us more than results. I also appreciate very much that I was given the opportunities to go to various conferences and talk to colleagues throughout the world.

I feel very lucky to have Dr.Mintsev taught me and help me in my first year in this group. His knowledge in physics and experiences in experiments helped me to start from a nearly blank experiment background. Working together for almost 6 years, Aaron Hammack helped me a lot. I also benefit a lot from our discussion on physics, technology and other important problems in the world.

Professor Fogler not only helped me a lot on theory but also gave me many important advices on research. I would also thank Professor Levitov, Professor Simons, Professor Sham and Dr.Keeling for collaboration and discussions. I am greatly thankful to Professor Gossard for high quality samples and discussions. These works cannot be done without such high quality samples.

I would like to thank Erik, Greg and Katya for helping me in experiments, Jason, Alex, Mikas, Yulia and Joe for physics discussions. Jeff and his colleagues in physics maintenance team, Valeri, Edwina and their colleagues in purchasing team, Debra and Hilari all helped me a lot, I would like thank all of them.

During 7 years in San Diego, I was taken great care by Aunt Amy, Hanna and their families. I would also thank my roommates Wang Yao, Chin Hsia and their families for great times we had together.

Finally, I want to express my deepest gratitude to my parents and my wife Zaoli

for their continuous support in pursuing my career goals.

The text of chapter 4, in part, is a reprint of the material as it appears in Sen Yang, L.V. Butov, L.S. Levitov, B.D. Simons, and A.C. Gossard, *Kinetics of the exciton ring and macroscopic ordered exciton state*, where the dissertation author was the first author. The co-authors in these publications directed, supervised, and co-worked on the research which forms the basis of this chapter.

The text of chapter 5, in part, is a reprint of the material as it appears in Sen Yang, A.V. Mintsev, A.T. Hammack, L.V. Butov, and A.C. Gossard, *The Role of Interaction in the Formation of Macroscopic Ordering in Exciton Rings*, Phys. Rev. B **75**, 033311, © 2007 The American Physical Society, where the dissertation author was the first author. The co-authors in these publications directed, supervised, and co-worked on the research which forms the basis of this chapter.

The text of chapter 5, in part, is a reprint of the material as it appears in Sen Yang, L.V. Butov, L.S. Levitov, B.D. Simons, and A.C. Gossard, *Commensurability of macroscopic exciton density wave*, where the dissertation author was the first author. The co-authors in these publications directed, supervised, and co-worked on the research which forms the basis of this chapter.

The text of chapter 6, in part, is a reprint of the material as it appears in Sen Yang, A.T. Hammack, M.M. Fogler, L.V. Butov, and A.C. Gossard, *Coherence Length of Cold Exciton Gases in Coupled Quantum Wells*, Phys. Rev. Lett. **97**, 187402, © 2006 The American Physical Society, where the dissertation author was the first author. The co-authors in this publication directed, supervised, and co-worked on the research which forms the basis of this chapter.

The text of chapter 6, in part, is a reprint of the material as it appears in M.M. Fogler, Sen Yang, A.T. Hammack, L.V. Butov, and A.C. Gossard, *Effect of spatial resolution on the estimates of the coherence length of excitons in quantum wells*,

Phys. Rev. B **78**, 035411, © 2008 The American Physical Society, where the dissertation author was the second author. The co-authors in this publication directed, supervised, and co-worked on the research which forms the basis of this chapter.

VITA

1980	Born, Qingdao, P. R. China
2002	Bachelor of Science Tsinghua University, Beijing, P. R. China
2002–2003	Teaching Assistant, Department of Physics University of California, San Diego
2004–2009	Research Assistant, Department of Physics University of California, San Diego
2009	Doctor of Philosophy University of California, San Diego

PUBLICATIONS

A.T. Hammack, N.A. Gippius, Sen Yang, G.O. Andreev, L.V. Butov, M. Hanson, and A.C. Gossard, *Excitons in electrostatic traps*, cond-mat/0504045 (2005);Appl. Phys. **99**, 066104 (2006).

A.L. Ivanov, L.E. Smallwood, A.T. Hammack, Sen Yang, L.V. Butov, and A.C. Gossard, *Origin of the inner ring in photoluminescence patterns of quantum well excitons*, cond-mat/0509097 (2005); Europhys. Lett. **73**, 920-926 (2006).

Sen Yang, A.T. Hammack, M.M. Fogler, L.V. Butov, and A.C. Gossard, *Coherence Length of Cold Exciton Gases in Coupled Quantum Wells*, cond-mat/0606683 (2006). Phys. Rev. Lett. **97**, 187402 (2006).

Sen Yang, A.V. Mintsev, A.T. Hammack, L.V. Butov, and A.C. Gossard, *The Role of Interaction in the Formation of Macroscopic Ordering in Exciton Rings*, cond-mat/0608342 (2006). Phys. Rev. B **75**, 033311 (2007).

Y.M. Shen, L. Pang, Y. Fainman, M. Griswold, Sen Yang, L.V. Butov, L.J. Sham. *Photoluminescence and spectral switching of single CdSe/ZnS colloidal nanocrystals in poly(methyl methacrylate)*, cond-mat/0703799 (2007), Phys. Rev. B **76**, 085312 (2007).

M.M. Fogler, Sen Yang, A.T. Hammack, L.V. Butov, and A.C. Gossard, *Effect of spatial resolution on the estimates of the coherence length of excitons in quantum wells*, cond-mat/0804.2686 (2008). Phys. Rev. B **78**, 035411 (2008)

J.R. Leonard, Sen Yang, L.V. Butov, and A.C. Gossard, *Spin transport of indirect excitons in GaAs coupled quantum wells*, cond-mat/0808.2402 (2008).

ABSTRACT OF THE DISSERTATION

Spontaneous coherence, kinetics and pattern formation in cold exciton gases in GaAs/AlGaAs Coupled Quantum Wells

by

Sen Yang
Doctor of Philosophy in Physics
University of California San Diego, 2009
Professor Leonid V. Butov, Chair

Indirect excitons in GaAS/AlGaAs coupled quantum wells have small mass, long lifetime and short cooling time. Those enable us to create a cold exciton gas. I will present the experimental study of this cold exciton gas including kinetics, pattern formation and coherence. A spatial photoluminescence pattern including external exciton rings, localized bright spots, and the macroscopically ordered exciton state (MOES) was observed. While the external ring is a classical object by itself it is the region where the coldest exciton gas is created: the external ring is far from the hot excitation spot and the excitons in the ring are formed from well-thermalized carriers. The MOES - an array of beads with spatial order on macroscopic length appears abruptly in the ring at temperatures below a few Kelvin, where the thermal de Broglie wavelength is comparable to the interparticle separation and the exciton gas is nonclassical. We performed the first time-resolved kinetics measurements in this system. Simulations based on in-plane charge separation model gave good agreements with experimental results. From the simulation fits, diffusion constant of electrons and holes were obtained. We also observed commensurability in MOES: the exciton density wave is stable when there is an integer number of MOES wavelength

between defects. In the external ring, a strong enhancement of spatial coherence length is observed below a few Kelvin. The increase of the coherence length is correlated with the macroscopic spatial ordering of excitons. The coherence length at the lowest temperature corresponds to a very narrow spread of the exciton momentum distribution, much smaller than that for a classical exciton gas.

Chapter 1

Introduction

1.1 Motivation

In 1925, Einstein predicted that a boson gas could condense into the lowest state when temperature of that gas is below certain critical temperature. This prediction is the result of Bose Einstein distribution, and the phenomenon is called Bose Einstein condensation (BEC). In 1995 several groups in the world announced the realization of BEC in atom cloud. Since then, study on BEC growing rapidly into a big field. Quantum coherence were demonstrated in matter wave interference [6], atom laser [58], optical lattice [29] etc. The prospective of making quantum simulator with BEC is high.

An exciton is a quasi particle made of an electron and a hole, it is a boson. Over 40 years ago, Keldysh and Kozlov [43] predicted the condensation of exciton. Exciton in bulk Cu_2O was a promising direction, because the ground state is optical inactive. But later people found the Auger recombination effect is too strong in that system, so the density cannot reach critical value. On the other side, indirect exciton in coupled quantum wells has more advantages, it is light, long lived, and has fast cooling rate. The particle interaction is repulsive, which is required for BEC. There

are also several features in this system: many parameters are in-situ tunable, for example density of exciton, lifetime, potential shape, temperature, etc. The critical temperature of BEC is also 6 orders of magnitude higher than atom due to its small mass. From the perspective of application, semiconductor industry is more mature than atom industry in manufactory.

The purpose of our study is to create a cold quantum exciton gas and probe its low temperature properties including coherence, interaction, kinetics and pattern formation.

1.2 Dissertation outline

In Chapter 2 we briefly review the properties of Bose Einstein condensation.

In Chapter 3 we briefly review the electron and exciton properties in GaAs/AlGaAs quantum wells. Cooling mechanism is explained. Then we introduce indirect exciton and show why we can use indirect exciton to create cold quantum gas. In the end, we discuss about the critical temperature of BEC in this 2D system.

Spatial photoluminescence (PL) patterns have been observed in coupled quantum wells. In Chapter 4 we introduce the external exciton rings, the localized bright spots (LBS) and the macroscopically ordered exciton state (MOES). The model of in-plane charge separation is introduced as the origin of external ring and LBS ring. We present the first time-resolved kinetics measurements in this system. Simulation based on in-plane charge separation model gave good agreement with experiment. Diffusion constant of electrons and holes are obtained from the simulation fits.

In Chapter 5 we present the experiment that determined: the interaction between indirect excitons is repulsive. So attraction cannot be the origin of MOES. A model based on stimulated scattering is introduced. This model fits with all experimental results. In the end we shows the experimental measurements on commensurability in MOES: exciton density wave is stable when there is an integer number of MOES

wavelength between defects.

In Chapter 6 we present two ways of measuring spatial coherence of exciton. A strong enhancement of spatial coherence length is observed below a few Kelvin, much larger than that for a classical exciton gas. The increase of the coherence length is correlated with the macroscopic spatial ordering of excitons. The coherence length at the lowest temperature corresponds to a very narrow spread of the exciton momentum distribution, much smaller than that for a classical exciton gas.

Chapter 2

A Brief Review on Bose Einstein Condensation

Let's use an ideal model: non-interacting boson gas. [35, 63]

For the grand canonical ensemble of bosons, the grand partition function is

$$Q(z) = \sum_{N=0}^{\infty} z^N \sum_{n_p} e^{-\beta \sum_p \epsilon_p n_p} = \sum_{N=0}^{\infty} \sum_{n_p} \prod_p (z e^{-\beta \epsilon_p})^{n_p} \tag{2.1}$$

here $N = \sum_p n_p$

So:

$$Q(z) = \prod_p \sum_n (z e^{-\beta \epsilon_p})^n \tag{2.2}$$

for bosons, n=0,1,2,3....., So the grand partition becomes:

$$Q(z) = \prod_p \frac{1}{1 - z e^{-\beta \epsilon_p}} \tag{2.3}$$

The average occupation number is given by

$$f = -\frac{1}{\beta} \frac{\partial}{\partial \epsilon_p} ln Q = \frac{1}{1/z e^{\beta E} - 1} \tag{2.4}$$

This is Bose Einstein distribution. $z = e^{\beta\mu}$. μ is chemical potential, $\beta = 1/k_B T$

Taking into account of density of states $g(E)$, the distribution function becomes:

$$f = \frac{g(E)}{e^{(E-\mu)/kT} - 1} \tag{2.5}$$

The chemical potential is determined by the density of particles $n = N/V$. When n increase, μ rises up. The highest chemical potential for bosons is the energy of lowest state. Otherwise the occupation number is that state is negative and unphysical for Bose Einstein distribution. Let us set the energy of lowest state is 0. So the total occupation numbers in excited states are:

$$\int \frac{g(E)}{e^{E/kT} - 1} dE \tag{2.6}$$

When total number of particles is more than total occupation numbers in excited states, bosons will accumulate in the lowest states, this is Bose Einstein condensation. So it is a condensation in momentum space.

So the condition for BEC is:

$$N \geq \int \frac{g(E)}{e^{E/kT} - 1} dE \tag{2.7}$$

To get the critical temperature, we need to know the density of states.

Density of states is defined as

$$g(E) = \frac{dN_s}{dE} \tag{2.8}$$

here N_s is the total number of states.

In free space, $E = \frac{p^2}{2m}$, in 3 dimension, N_s is the volume of a sphere with radius p, so $N_s = \frac{4}{3}\pi p^3 \frac{V}{(2\pi\hbar)^3} = \frac{4}{3}\pi (2mE)^{3/2} \frac{V}{(2\pi\hbar)^3}$. so density of states is

$$g(E) = \frac{dN_s}{dE} = 2\pi (2m)^{3/2} \frac{V}{(2\pi\hbar)^3} \sqrt{E} \tag{2.9}$$

the critical temperature should satisfy:

$$N = \int \frac{g(E)}{e^{E/kT_c} - 1} dE = \frac{m^{3/2} V}{2^{1/2} \pi^2 \hbar^3} \int \frac{\sqrt{E}}{e^{E/kT_c} - 1} dE \tag{2.10}$$

for dimension n space, N_s is the volume of n dimension sphere, so $N_s \sim p^n = (2mE)^{\frac{n}{2}}$.

$$g(E) = \frac{dN_s}{dE} \sim E^{\frac{n}{2}-1} \tag{2.11}$$

$$N = \int \frac{g(E)}{e^{E/kT_c} - 1} dE \sim \int \frac{(2mE)^{\frac{n}{2}-1}}{e^{E/kT_c} - 1} dE \tag{2.12}$$

In 3-D case, the critical temperature can be solved as $kT_c = 3.31 \frac{\hbar^2 n^{2/3}}{m}$

In 2-D case, the integral diverge. It was shown that this is due to the long wavelength thermal fluctuation of phases. It destroyed the long range order in 2D ([34]).

But in finite 2D system, the states are discrete, the first excited state has a energy gap $E_m \sim \frac{\hbar^2}{mS}$, S is the area.

So the total number of particles in excited states becomes:

$$N_{ex} = \int_{E>E_m} \frac{1}{e^{E/kT} - 1} dE = \frac{kT}{E_m} ln(\frac{kT}{E_m}) \tag{2.13}$$

When $N_{ex} = N$, the transition starts, so the critical temperature is:

$$T_c \sim \frac{\hbar^2 n}{mklnN} \tag{2.14}$$

That means the critical temperature is lnN smaller than the de Broglie temperature, at which temperature de Broglie wavelength is comparable to the particle separation. Below T_c the small momentum particles contribute to a so-called quasi-condensate, which results in the appearance of superfluidity. The difference between the quasi-condensate and the Bose-Einstein condensate is not essential for most experiments [64] and distinguishing between them unambiguously in experiments is hard (if possible).

Chapter 3

Properties of excitons in GaAs CQW : A Brief Review

3.1 Introduction to exciton

Laser can excite an electron into conduction band while leave a hole in valence band. There is Coulomb attraction between electron and hole. When temperature is below the binding energy, exciton which is an electron hole pair can be formed.

In out experiments excitons are in GaAs coupled quantum wells. Let us start from band structure of GaAs.

Fig. 3.1 shows the band structure of GaAs. Conduction band electron is in s-orbital like state. $s_e = \frac{1}{2}$, $j_e = \frac{1}{2}$.

Valence band hole is like a p wave particle. So $l = 1$, and $s = \frac{1}{2}$, so $j = l + s$ could have two possible values $j = \frac{1}{2}$ and $j = \frac{3}{2}$. The energy difference between those states are mainly due to spin-orbital interaction, which is governed by:

$$E_{so} \sim l \cdot s \sim j^2 - (s^2 + l^2) \tag{3.1}$$

The energy difference between $j = \frac{1}{2}$ and $j = \frac{3}{2}$ is around 360meV, this is so

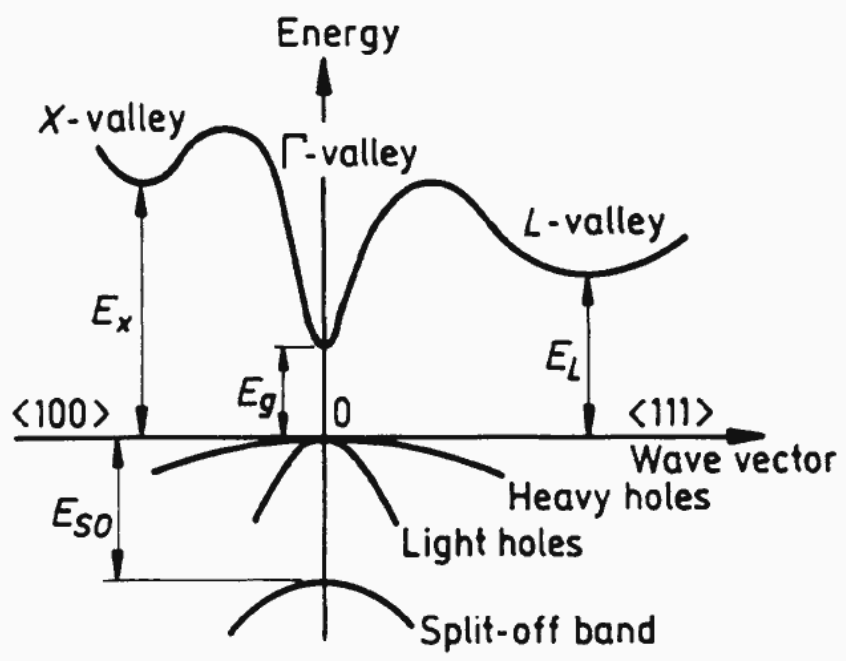

Figure 3.1: Bulk GaAs band structure.

called split-off band. It odes not contribute to our experimental results.

For $j = \frac{3}{2}$, there are two states $j_z = \pm\frac{3}{2}$ and $j_z = \pm\frac{1}{2}$, which are called heavy hole and light hole. This is due to the difference in effective mass.

For bulk GaAs, for $k = 0$, heavy hole state has the same energy as light hole, because of spatial reverse symmetry. But in quantum wells, in $k = 0$, heavy hole light hole energy difference due to z direction reverse symmetry breaking. Fig. 3.2 shows GaAs/AlGaAs quantum well valence band structure.

When hole and electron form exciton, there are light hole exciton and heavy hole exciton, the energy difference between light hole exciton and heavy hole exciton is around 20meV. In experiments in this thesis, the exciton is heavy hole exciton.

Fig. 3.3 shows the dispersion of exciton. Not all excitons are optical active. In 3-D, because of momentum and energy conservation, only the state ,where exciton

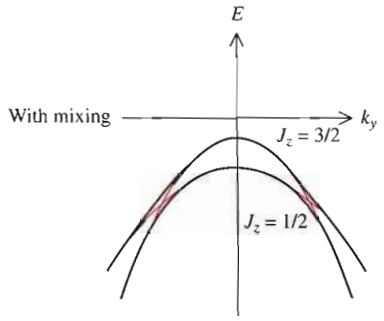

Figure 3.2: GaAs/AlGaAs quantum well valence band structure [88]

dispersion and photon dispersion meet, can directly emit light. For quantum wells, z direction momentum conservation is broken, so all states lower than that state can directly radiate. This height of light cone is around 0.1meV, i.e. 1K.

When hole and electron form exciton, angular momentum in z direction is equal to $m_X = j_{e,z} + j_{h,z}$, $j_{e,z} = \pm\frac{1}{2}$, $j_{h,z} = \pm\frac{3}{2}$, the there are 6 possible excitons $m_X = 0$, $m_X = \pm 2$ and $m_X = \pm 1$. For quantum wells, z direction is the growth direction, the rotation system is still conserved in z direction, while in x and y direction, it is not conserved anymore. So when electron and hole in exciton recombine into photon, z direction angular momentum and energy have to be conserved (for bulk, total angular momentum $j_X = j_e + j_h$ has to be conserved, so states with $j = 2$ are dark states). Therefore, $m_X = \pm 2$ exciton can only emit a photon by the help of another photon or phonon to fulfill this requirement, this rate is very low. So $m_X = \pm 2$ is called dark state, while $m_X = \pm 1$ state is called bright state. $m_X = 0$ will emit in a direction in x-y plane, because we collect light emitted within α angle to z axis (here α is defined by the objective numerical aperture $N.A. = sin\alpha$, for our experiment setup, $\alpha = 16°$), we cannot collect light emitted by $m_X = 0$ state exciton.

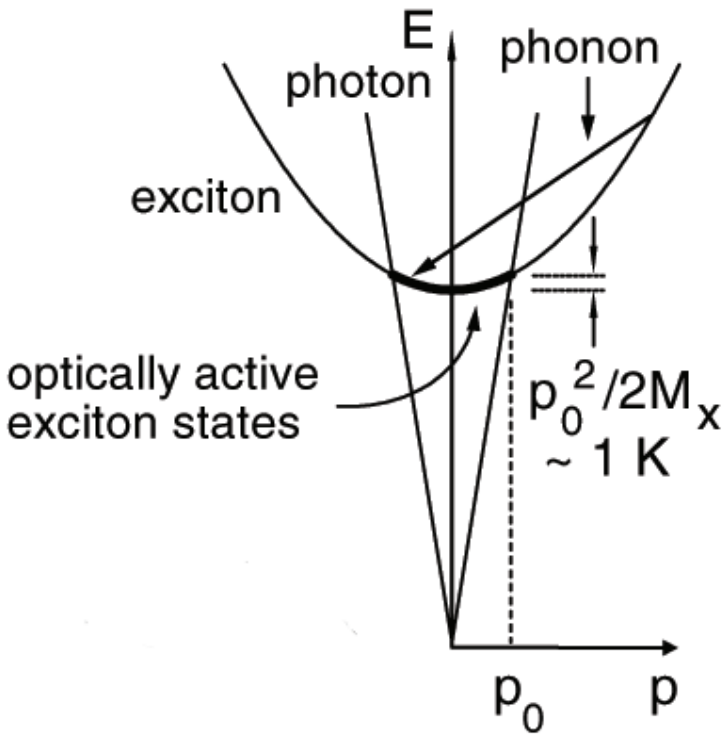

Figure 3.3: Exciton dispersion and radiation zone [15]

3.2 Cooling for the excitons

Cooling lattice temperature is relative easy. Regular helium-4 cryostat can go down to 1.5K, helium refrigerator can go below 50mK.

To realize a cold exciton gas, lifetime of exciton should be longer than cooling time.

The cooling of exciton is mainly due to phonon emission. He-Ne laser is 400meV above the resonate energy. When laser hits sample, it creates hole and electron plasma. This plasma is cooled down by emitting optical phonons. The energy

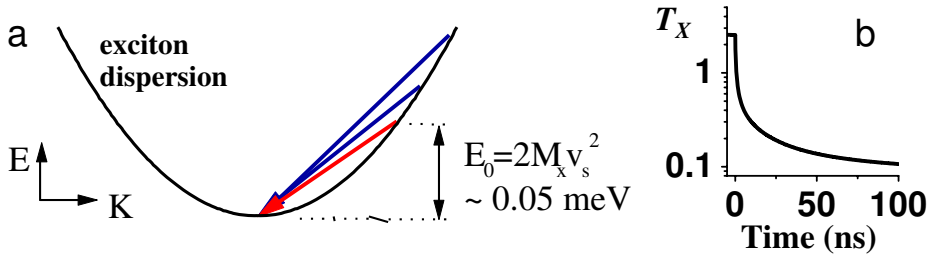

Figure 3.4: Cooling scheme. (a) scheme of exciton cooling by phonon emission. [15] (b) theoretical calculation of exciton temperature versus cooling time [12]

of optical phonon is around 36meV. Below 360K, the cooling mechanism becomes mainly low energy acoustic phonons.

In bulk, due to conservation of both momentum and energy, only excitons with energy $E = 2Mv_s^2$ (v_s is speed of sound) can couple with the lowest exciton state by a phonon emission. In quantum wells, due to symmetry breaking in z direction, z direction momentum is not conserved any more. So excitons with energy higher than $E = 2Mv_s^2$ can be scattered into lowest state by a phonon. The cooling time is orders of magnitude faster than cooling time in bulk. Theoretical calculation shows exciton temperature can drop down to 400mK in about 5 ns [12]. So if we can get exciton with long enough lifetime, it can be cooled down.

3.3 Indirect exciton

Fig. 3.5 shows the structure of our sample. An electric-field-tunable $n^+ - i - n^+$ GaAs/(Al,Ga)As CQW structure was grown by molecular beam epitaxy. The i-region consists of two 8 nm GaAs QWs separated by 4 nm $Al_{0.33}Ga_{0.67}As$ barrier and surrounded by two 200 nm $Al_{0.33}Ga_{0.67}As$ barrier layers. The n^+-layers are Si-doped GaAs with $N_{Si} = 5 \times 10^{17}$ cm^{-3}. The electric field in the z-direction is created by the external gate voltage V_g applied between n^+-layers $E = V_g/D$.

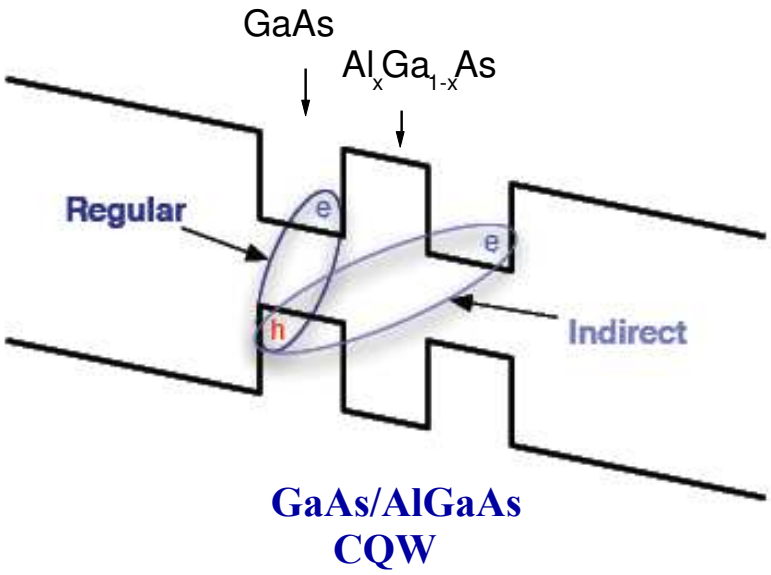

Figure 3.5: Sample structure and scheme of direct exciton and indirect exciton.

There are two kinds of excitons in this structure: direct exciton and indirect exciton. Direct exciton is an exciton with both electron and hole in the same quantum well, while indirect exciton has electron and hole in separated quantum wells. Due to this spatial separation, the life time of indirect exciton is orders of magnitude longer than that of direct exciton. The lifetime of direct exciton is around 10ps, while indirect exciton life time varies with the gate voltage, typical in the order of tens of ns in experiments ($V_g \sim 1.2V$). So indirect exciton has enough lifetime to be able to cool down to low temperature, while direct exciton cannot reach thermal equilibrium and stay hot.

Energy of direct exciton and indirect exciton depends on z direction electric field differently, because indirect exciton is a dipole in z direction while direct exciton is not. So energy of indirect exciton $\epsilon_D = E_g - E_D$, energy of indirect exciton $\epsilon_I = E_g - E_I - eEd$. Here E_g is band gap. E_D and E_I are binding energy of direct

exciton and indirect exciton, $E_D \sim 10meV$ and $E_I \sim 5meV$ in this sample. d is the interlayer separation, around $11.5\mu m$ in this sample. With small gate voltage, direct exciton is energy favorite, with high gate voltage, indirect exciton is energy favorite. In typical experiment, gate voltage is around 1.2V, indirect exciton line is at 801nm, while direct exciton line is 789nm, the energy difference is roughly 20meV.

Because there is energy difference between direct and indirect exciton, the population difference between these two states can be used as a thermometer. The energy difference between direct and indirect exciton is roughly 20meV, corresponds to 200K. So if population of direct exciton is observed, that means that place is hot. But direct exciton has short lifetime, too short to reach thermal equilibrium, so the formulae $\frac{N_D}{N_I} = e^{-\frac{\Delta E}{k_B T}}$ is not accurate below ∼20K. More accurate temperature measurement can be done by observing if PL intensity rising up after laser off. Because the height of radiation zone is only 1K. If exciton temperature is higher than that, many excitons are in optical inactive state, when laser turns off, those exciton will fall to radiation zone to emit light, that creates a rising up in PL intensity.

The linewidth of indirect exciton is around 1.2meV, direct exciton linewidth is almost the same, slightly smaller. Linewidth broadening comes from many ways, including homogeneous broadening, such as spontaneous emission (lifetime of exciton), exciton scattering, and inhomogeneous broadening, such as localization and interaction with charged defect [53]. Because indirect exciton is a dipole and thus more sensitive to defects, the almost same linewidth of direct and indirect exciton shows the charge defect does not play a big role in our sample. Experiments in [33, 68] show disorder potential is below 0.4meV, so it is also not the main mechanism of line broadening. The sharp line experiment in elevated trap shows interaction between excitons is the main cause of line broadening [33].

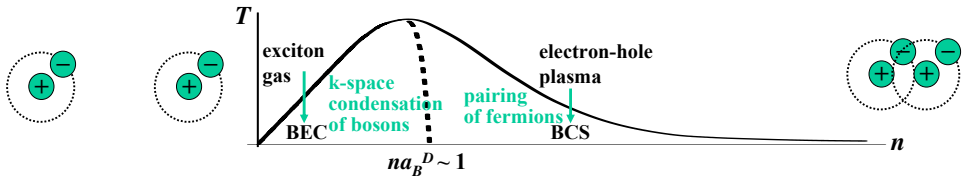

Figure 3.6: Phase diagram of exciton system, in low density side, the system is either exciton gas or exciton BEc, in high density side, the system is either electron hole plasma or BCS like state.

3.4 Phase diagram

Indirect exciton has relative smaller lifetime than atoms. But its lifetime is longer than its cooling time, so exciton gas is in thermal equilibrium. BEC and other conclusions derived from statistical mechanics in Chapter 2 are still valid.

Keldysh and Kozlov [43] showed that in the dilute limit ($na_B^D \ll 1$, where a_B is the exciton Bohr radius, n is the exciton density, and D is the dimensionality) excitons are weakly interacting Bose particles and are expected to undergo Bose-Einstein condensation (BEC). In the opposite limit of a dense e-h system ($na_B^D \gg 1$) excitons are analogous to Cooper pairs. It is called the excitonic insulator, and it is analogous to the BCS superconductor state [42]. Here the pairing is due to electron hole attraction. Because electron hole pair is neutral, so this BCS like state is an insulating state. At $na_B^D \sim 1$ cross over between BEC/exciton gas and BCS/plasma state happened. Bohr radius for indirect exciton is 20nm, so critical transition density (Mott density) $n_{Mott} \sim \frac{1}{a_B^2} \sim 2^{11} cm^{-2}$. Above this density, exciton will dissociate due to phase space filling and screening. In experiment we did, the typical density is around $10^9 - 10^{10} cm^{-2}$.

Fig. 3.6 shows the phase diagram of exciton system. In low density side, the system is either exciton gas or exciton BEC, in high density side, the system is either electron hole plasma or BCS like state. All our experiments were performed

in low density side, so in high temperature exciton is in the state of exciton gas, in low temperature it is in exciton BEC state.

The BEC transition temperature depends on particle mass. In our sample, exciton mass $M_X = 0.22m_e$, several orders of magnitude smaller than mass of atom, so the critical temperature is much higher.

The de Broglie temperature T_{dB} at which the thermal de Broglie wavelength $\lambda_{dB} = \sqrt{2\pi\hbar^2/(mk_BT)}$ is comparable to the interexcitonic separation, i.e. $\lambda_{dB}^2 n/g = 1$, is given by $T_{dB} = 2\pi\hbar^2 n/(k_B M_x g) \approx 3K$. Below this temperature, the occupation number in ground state becomes bigger than 1. Excitons start to form quasi-condensate.

The critical temperature of complete condensation of N particles will be $\frac{T_{dB}}{lnN}$. For a spot size $20\mu m$ with density $10^{10}cm^{-2}$, the critical temperature is around 0.2K.

For indirect exciton with long life time and fast cooling speed, this temperature can be realized in dilution fridge, in which the bulk temperature can be lower than 0.09K.

Chapter 4

Pattern formations in cold exciton gas

4.1 Introduction to external ring and LBS

Fig. 4.1a is the real space PL of indirect exciton emission. Sample is excited off-resonantly by 632nm He-Ne laser. When sample is excited at lowest excitation powers P_{ex}, the spatial profile of the indirect exciton PL intensity, practically follows the laser excitation intensity. However, at high laser power, the indirect exciton PL pattern is characterized by a ring structure: the laser excitation spot is surrounded by two concentric bright rings separated by an annular dark inter-ring region (Fig. 4.1) . The rest of the sample outside the external ring is dark. The internal ring appears near the edge of the laser excitation spot and its radius reaches tens of μm. The external ring can be remote from the excitation spot by more than 100 μm. Its radius increases with P_{ex}. The ring structure follows the laser excitation spot when it is moved over the whole sample area. When the temperature is increased, the bright rings wash out gradually and the PL profile approaches a monotonic bell-like shape. The spatial pattern shows also that the indirect exciton PL intensity is strongly

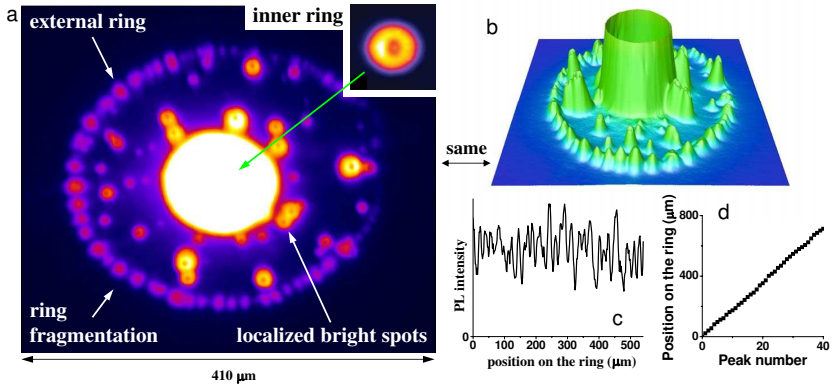

Figure 4.1: (a-b) The spatial pattern of the indirect exciton PL. [50] (c) PL intensity profile along the ring. (d) peak position along the ring versus peak number. [13]

enhanced in certain fixed spots on the sample called localized bright spots (LBS). For any excitation spot location and any P_{ex} the LBS are only observed when they are within the area terminated by the external ring. In the LBS the indirect exciton PL line is spectrally narrow, $FWHM \quad 1.2meV$. The external ring is fragmented into circular-shape structures that form a periodic array over macroscopic lengths, up to 0.5mm (Fig. 4.1c). This is demonstrated in Fig. 4.1d, which shows the nearly linear dependence of the fragment positions along the ring versus their number. The in-plane potential fluctuations are not strong enough to destroy the ordering . The fragments follow the external ring either when the excitation spot is moved over the sample area or when the ring radius varies with P_{ex}. Along the whole external ring, both in the peaks and the passes, the indirect exciton PL lines are spectrally narrow with the full-width at half-maximum1.2 meV, considerably smaller than at the center of the excitation spot. The ring fragmentation into the periodic chain appears abruptly at low temperatures below 3K; this is quantified by the amplitude of the Fourier transform of the PL intensity variation along the ring (Fig. 4.2d). Each fragment contains a macroscopic number of excitons which can exceed tens of thousands and the period of the fragmentation varies within the macroscopic length

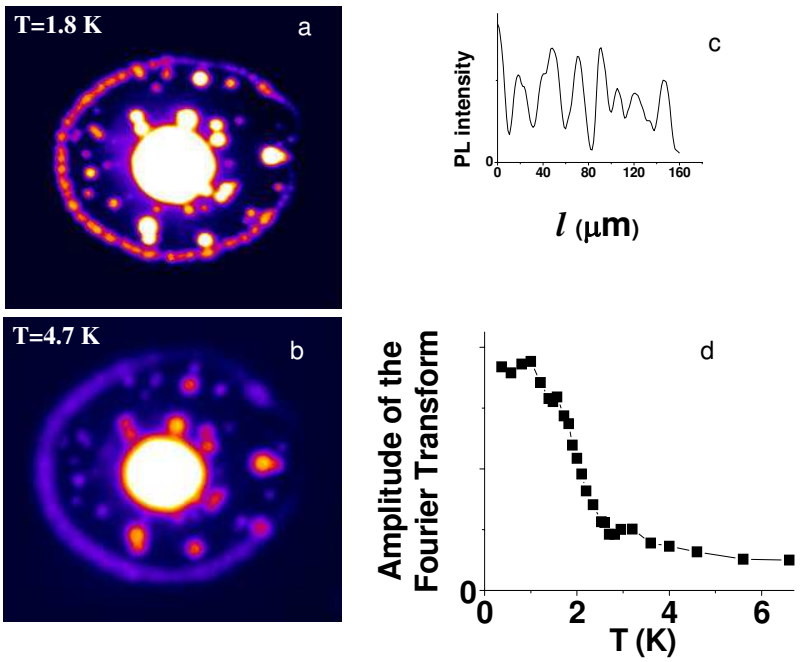

Figure 4.2: (a),(b) The spatial pattern of the indirect exciton PL at lattice temperature $T = 1.8K$(a) and $T = 4.7K$(b). (c) PL intensity profile along the ring. (d) Exciton density Fourier transform peak height at the fragmentation period vanishes continuously at a critical temperature. [17]

scale, 10-50 μm. We call the exciton state with spatial order on macroscopic length scale the macroscopically ordered exciton state (MOES).

The origin of this MOES will be discussed in next chapter. In this chapter we will discuss the origin of this external ring and LBS rings.

4.2 Model of in-plane charge separation

In principle, excitons can travel in a dark state after having been excited until slowed down to a velocity below photon emission threshold, where they can decay radiatively. This is the origin of inner ring which is around tens of microns away from

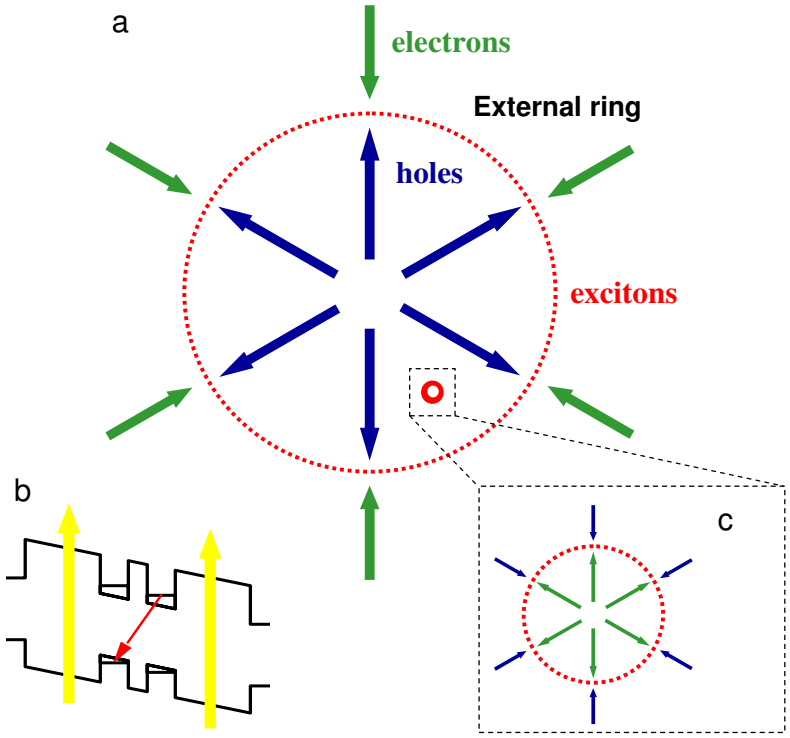

Figure 4.3: Scheme of external ring (a) and LBS (c) model. Electron-rich region, hole-rich region, and exciton ring are indicated. (b) scheme of off-resonate laser excitation

the laser spot. But this cannot explain for external ring, for example, external ring is sharp in edges, also the radius of external ring strongly depends on gate voltage, with small change in gate voltage, the ring radius changes a lot.

The transportation of exciton cannot explain external ring, it is assumed that excitons are generated in the ring [16, 66]. 632nm He-Ne laser was used to excite the sample. The laser frequency is even above the $Al_{0.33}Ga_{0.67}As$ barrier band gap ($\sim$645nm). So equal number of electrons and holes are generated in every layer in the sample (Fig. 4.3b). Electrons and holes will drift under z direction electrical field due to applied gate voltage. Mass of holes is heavier than mass of electrons,

so the quantum well collection efficiency of holes is higher than that of electrons. More holes are collected in quantum wells than electrons. In the quantum well, holes drift and diffuse outwards from laser spot, bind with electrons, form indirect excitons. This process depletes electrons in the vicinity of the laser spot, creating an essentially electron-free and hole rich region, which allows holes to travel a relatively large distance without encountering electrons.(Fig. 4.3a).

At the same time, a spatial non-uniform electron distribution builds up, causing a counterflow of electrons towards the laser spot. A sharp interface between the hole rich region and electron rich region is formed (Fig. 4.3a). Excitons are formed in this interface. This is the origin of external ring.

The model can be written as the following equations:

$$\begin{cases} \partial_t n = D_{\mathrm{e}} \nabla^2 n - wnp + J_{\mathrm{e}}, \\ \partial_t p = D_{\mathrm{h}} \nabla^2 p - wnp + J_{\mathrm{h}} \\ \partial_t n_{\mathrm{x}} = D_{\mathrm{x}} \nabla^2 n_{\mathrm{x}} + wnp - \gamma_x n_{\mathrm{x}} \end{cases} \tag{4.1}$$

n,p,n_x are electron, hole, exciton densities. D_{e}, D_{h} and D_{x} are electron, hole, exciton diffusion constants. w is the formation rate of excitons. γ_x is the recombination rate of excitons. J_h is the hole source term. Because holes are created by laser excitation, so hole source is localized at the excitation spot, i.e. $J_h = P_{ex}\delta(r)$. Electron source is everywhere in the sample. Net electron current coming into quantum well $J_e = I(r) - \gamma(r)n(r)$, $I(r)$ is the current into quantum well, $\gamma(r)$ is the tunneling rate of electrons, $\gamma(r)n(r)$ is the current tunneling out of quantum well. When there is no light, current into quantum well should be equal to current out. So $I(r) = \gamma(r)n_b(r)$, $n_b(r)$ is the background electron density in quantum well.

Current into the quantum well is not uniform in the quantum well plane. There are some small current filaments. Those are defects in the sample. Their positions are fixed. Although the total current is still in the order of nA, the current filaments have much higher current compared with other part of the sample. They provide a

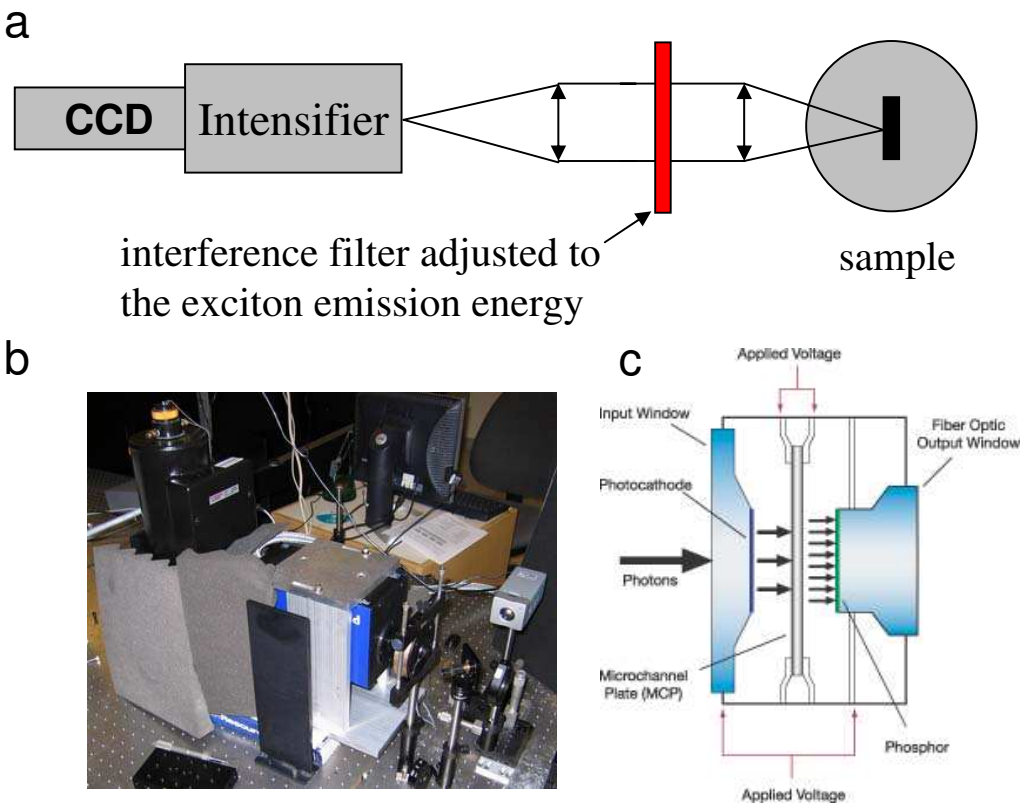

Figure 4.4: kinetics measurement setup, (a) scheme of experimental setup. (b) photo of Picostar HR-12 image intensifier. (c) structure of intensifier

electron-rich region near themselves. When defects are inside the external ring, i.e. surrounded by hole rich region, interface between hole rich region and electron rich region is formed near defects. Excitons are generated in that interface and form ring, that is the LBS ring (Fig. 4.3c).

4.3 Measurements

The observation of pattern formation [13] and the model [16] were made years ago. My project was to confirm this model by experiments. The way to confirm this

model is to use both time-resolved and spatial resolved measurement. This was done by using intensified ccd (ICCD) (Fig. 4.4b).

ICCD is made of a intensifier and a regular ccd with coupling optics. Fig. 4.4c shows the structure of intensifier. A image intensifier is a vacuum tube like device. It has a photocathode, a phosphor screen and a electron-multiplying microchannel plate (MCP). Photons strike the photocathode to generate electrons via the photoelectric effect. Those electrons are then accelerated by gate voltage across MCP. They hit the phosphor screen to release light (usually green light at 532nm). CCD coupled to this screen plane generates spatial resolved image. Time resolved measurement can be done by sending short gate voltage pulse to MCP, so only in certain time windows, the signal gets intensifier and through intensifier.

We use a Picostar HR-12 image intensifier from Lavision Gmbh. It uses Gen II single stage MCP. Photocathode is S25/18 mm. Spectral response of this photocathode is from 350-900nm. Photo gate can be from 300ps to 1ms. The gating Rep. Rate is up to 110MHz. Gating jitter is smaller than 20ps. Quantum efficiency is 10% at 800nm. Spatial resolution is 50-100μm. The detection is done with a 2048 x 512 nitrogen-cooled CCD. Here we use 20x magnification, so the spatial resolution in sample plane is 2-5 μm

Fig. 4.4a shows the experimental setup. We used a pulsed laser diode with center emission wavelength 635nm. The pulse duration was 10 μs, the edge sharpness <1 ns, and the repetition frequency 67KHz, i.e. 15 μs period (Fig. 4.5i). PL was collected by objective and spectral selection by an 800 ± 5 nm interference filter chosen to match the indirect exciton energy.

Fig. 4.5a-h shows images of emission of indirect exciton at different time delays. Image integration time is 200 ns. $t = 0$ corresponds to the end of the laser pulse. Let us start from the beginning, after laser turns on, external ring expands and saturates on the time scale of 1-3 μs, LBS rings appear after external ring pass by. After laser off, inner ring disappears in 50-100 ns, external ring shrinks on the time scale of 1 -

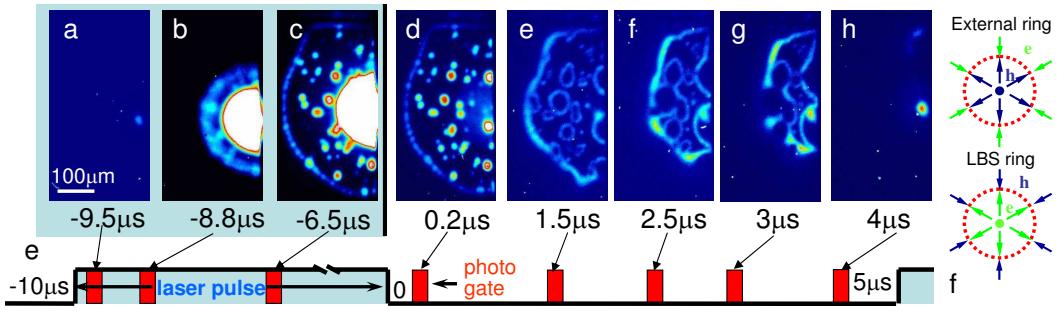

Figure 4.5: (a-h) Images of emission of indirect excitons at different time delays. Image integration time is 200 ns. $t = 0$ corresponds to the end of the laser pulse. (i) Scheme of laser excitation pulse and photo gates for the images in (a-h). Gate voltage V_g =1.235V, laser excitation peak power $P_{ex} = 1.82$ mW for the data. [83]

3 μs, while LBS rings start to expand and forms bigger ring. Eventually, all exciton signal disappears in around 3 μs. All these process can be explained by the model of in-plane charge separation. When laser turns on, holes are generated, they transport outwards to create a hole-rich region and push the interface between electron rich region and hole rich region outwards, until they are balanced by electrons tunneling into quantum well by gate voltage. After laser turns off, the hole flow starts to drop, electron flow from outside external ring starts to push the interface inward, while electrons flow in LBS start to push interface outwards. That is why external ring shrinks while LBS ring expands.

The time scale of inner ring kinetics is quite different from that of external ring and LBS ring. This also can be explained by the model. Inner ring is due to transportation of excitons created in laser excitation spot. When laser turns off, inner ring will disappear in the time scale of exciton lifetime, which is around tens of ns. This time scale is in agreement with the experiment. While external ring is formed by exciton formation in the interface between electron rich region and hole rich region. As long as there are electron-hole interface, electron flow and hole flow, there will be external ring. The time scale is determined by how long both flow can

last.

To analyze those results, ring radius versus delay time is plotted in Fig. 4.6a,b, experimental results showed in points. The ring radius is measured by calculating the area inside external ring. In Fig. 4.6a, 4 data sets corresponds to 4 different laser powers, $P_{ex} = 0.45, 0.76, 1.04$ and 1.82 mW at gate voltage $V_g = 1.235$ V. From the plot, we can see, with increasing laser power, both the ring radius and decay time increase. This is because higher laser power creates more holes. In Fig. 4.6b, 2 data sets corresponds to different gate voltage,$V_g = 1.22$ and 1.245 V at $P_{ex} = 0.76$ mW. From this plot, we can see, with increasing gate voltage, both ring radius and decay time decrease. This is because higher gate voltage increases tunneling rate of electron. The electron flow increases. Now we are going to use the model to simulate those results.

4.4 Simulations

Here we use a simplified model:

$$\begin{cases} \frac{dn}{dt} = D_n \nabla^2 n - wnp - \gamma(n - n_b), \\ \frac{dp}{dt} = D_p \nabla^2 p - wnp + I_p \delta(r). \end{cases} \tag{4.2}$$

We ignored the diffusion of excitons, only focused on transportation of electrons and holes. Now the model depends on diffusion constant of electron and hole D_n D_p, the formation rate of excitons w, source terms including tunneling rate of electron γ, initial background electron density n_b and laser excitation power I_p. We assume electron source is uniform everywhere in the sample, so γ and n_b are constants everywhere.

The physics values we want to fit are ring radius and decay time. Ring radius was measured at the time when laser is off, i.e. at delay time=0. The decay time is measured as the time it took the ring to shrink from maximum ring radius to half of

it. In Fig. 4.6d-o, we plot those two physics values' dependence on each parameter in the model. We can see both ring radius and decay time are strongly dependent on sources (Fig. 4.6i-o). This result agrees with experiment, changing either laser power or gate voltage will change the ring radius strongly. Changing formation rate of exciton w gives little change in ring radius and decay time (Fig. 4.6h,i). Ring radius and decay time is mildly depend on diffusion constant of electrons (Fig. 4.6f,g). While ring radius is not sensitive to diffusion contant of holes (Fig. 4.6d), decay time is strongly dependent on it(Fig. 4.6e). This is because electron source is everywhere in the sample, while holes are only created in laser spot and have to transport from there. So we can first fix sources by fitting ring radius, then fitting decay time by D_p.

In Fig. 4.6c, we present fitting results for P_{ex}=1.82mW data. The simulated results are presented by false color images, while the experimental data are present in points. We use the same source parameters in simulation and only change D_p. By comparing the decay time, D_p=26cm^2/s is the best fit.

With D_p fixed, we fit all 4 set of data in Fig. 4.6a with different laser sources, and 2 set of data in Fig. 4.6b with different tunneling rates. Also because external ring is the balance of electron flow and hole flow, when we change both electron flow and hole flow by the same ratio, the ring radius and decay time should remain fix [31], this can be seen in Fig. 4.6p,q. Here we change both γ and I_p up to two times, ring radius and decay time are only slightly changed.

Now let us discuss kinetics of LBS ring. After Laser turns off, LBS expands and form ring. In Fig. 4.7c,d, we plot ring radius of LBS ring versus delay time. In Fig. 4.7c, three data sets correspond to three different LBS marked in Fig. 4.7(a,b) by the arrows at V_g =1.235V and P_{ex}=1.82mW. Three LBS have different size as in Fig. 4.7(a). Because three LBS have roughly the same distance to laser spot, the hole density around them is the same. Different size corresponds to different electron flow in LBS. Bigger LBS has stronger electron flow. The LBS marked by green arrow is

the biggest, that means its electron flow is the strongest. This can be proved by the expansion process after laser turns off. Because with stronger electron flow, LBS ring expands faster. In Fig. 4.7c, LBS of green arrow which is the biggest expands the fastest, LBS with yellow arrow which is the smallest expands the slowest. This can be seen from different expansion speed of same LBS with different gate voltages. In Fig. 4.7d, two data sets correspond to the same LBS under two different gate voltage $V_g = 1.22$ and 1.245 V at $P_{ex} = 0.76$ mW. The LBS is marked in Fig. 4.7(a,b) by gray arrow. The laser power which corresponds hole flow is the same, different gate voltages correspond to different electron flow rate. Higher gate voltage generates stronger electron flow. The expansion speed is faster. We can use the similar model to simulate LBS ring.

$$\begin{cases} \frac{dn}{dt} = D_n \nabla^2 n - wnp - \gamma(n - n_b), \\ \frac{dp}{dt} = D_p \nabla^2 p - wnp. \end{cases} \tag{4.3}$$

The initial density of hole is p_b. Because LBS has a higher current than other part of the sample, n_b is not uniform in this model, inside LBS, $n_b = n_{b@LBS}$, in the other part of sample, $n_b = n_{b@other}$.

The model depends on D_p, D_n and source terms. We try to fit the expansion process by this model. It is not quite sensitive to D_p, because initially holes are everywhere. The electron and hole source ratio change the expansion process when LBS ring is within $5\mu m$ away from LBS as in Fig. 4.7c. After that the expansion speed is mainly determined by D_n. That means how fast the electron can move out. So we can fix the source by initial expansion and fix D_n by expansion after. In Fig. 4.7e, we show the fitting with different D_n for data in Fig. 4.7d with $V_g = 1.22$ V at $P_{ex} = 0.76$ mW. D_n=80cm^2/s is the best fit. Using those parameters we fit data in Fig. 4.7c,d. The tunneling rate we got from Fig. 4.7d is in agreement with the result from Fig. 4.6b.

This experiment is the first time-resolved and spatial-resolved measurement for

external ring and LBS ring. The results fit the model of in-plane charge separation. From the results we got diffusion constant of electrons and holes. This experiment shows another way to measure these two constants in this system.

From our results, D_n is 3 times higher than D_p. This is partially because electron is two times lighter than hole in this quantum well structure. Also because electron and hole are not in the same quantum wells, different localization and screening condition will contribute to the difference in diffusion. In [21], a similar ring formation was observed in a single quantum well structure. The result was explained by the same model. But the time of ring dynamics in that system is in the order of ms, three orders of magnitude longer than in our system. This may relate to different diffusion constant due to localization and screening.

4.5 Acknowledgements

The text of chapter 4, in part, is a reprint of the material as it appears in Sen Yang, L.V. Butov, L.S. Levitov, B.D. Simons, and A.C. Gossard, *Kinetics of the exciton ring and macroscopic ordered exciton state*, where the dissertation author was the first author. The co-authors in these publications directed, supervised, and co-worked on the research which forms the basis of this chapter.

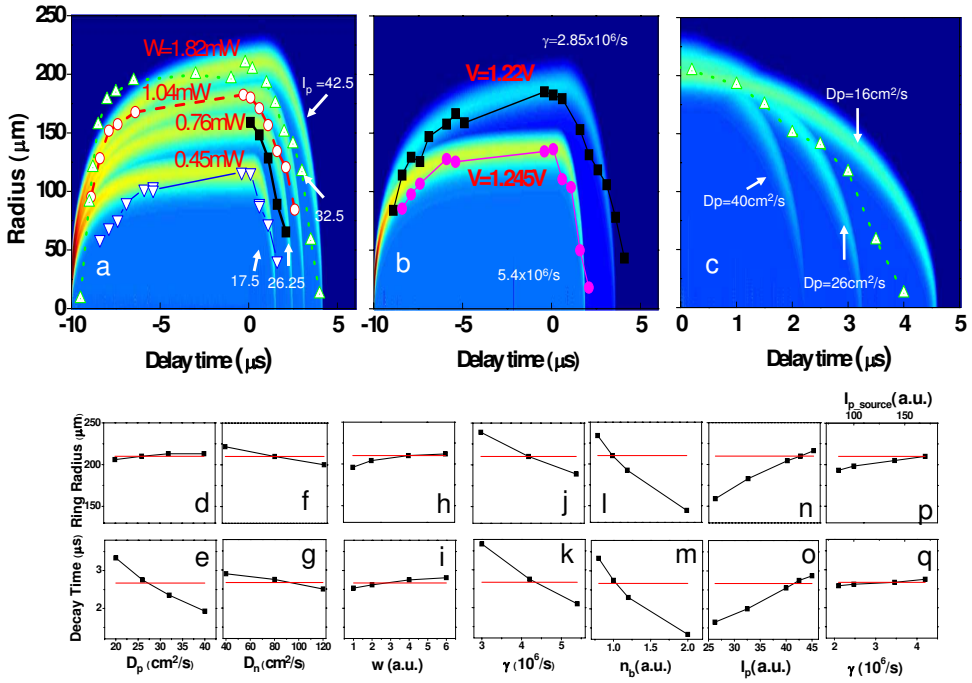

Figure 4.6: External ring kinetics. (a) Measured kinetics of the external ring radius for different excitation powers $P_{ex} = 0.45, 0.76, 1.04$ and 1.82 mW at gate voltage $V_g = 1.235$ V (points). The simulated kinetics for different $I_p = 17.5, 26.25, 32.5$ and 42.5 at $\gamma = 4.2 \times 10^6$ s^{-1} are presented by false color images. (b) Measured kinetics of the external ring radius for different $V_g = 1.22$ and 1.245 V at $P_{ex} = 0.76$ mW (points). The simulated kinetics for different $\gamma = 2.85$ and 5.4×10^6 s^{-1} at $I_p = 26.25$ are presented by false color images. $D_n = 80$ cm^2/s, $D_p = 26$ cm^2/s, $n_b = 1$, and $w = 4$ in the simulations in (a,b). (c) Comparison of simulated kinetics for different $D_p = 20, 26$ and 40 cm^2/s with the rest of the parameters same as in (a). $D_p = 26$ cm^2/s results to a better fit of the experimental kinetics for $P_{ex} = 1.04$ mW in (a). Here we shift the simulation result so that delay time=0 corresponds to the time when ring radius is maximum.(d-q)The dependence in external ring model parameters for ring radius and decay time. The parameters are diffusion constants D_p (d,e) and D_n (f,g), formation rate of exciton w (h,i). and sources including tunneling rate for electrons γ (j,k), n_b (l,m) and hole source I_p (n,o). γ and I_p are changed by the same ratio in (p,q). (p) The dependence of laser excitation power and gate voltage when ring radius is kept the same. The rest of the parameters in (d-q) are the same in (c). [83]

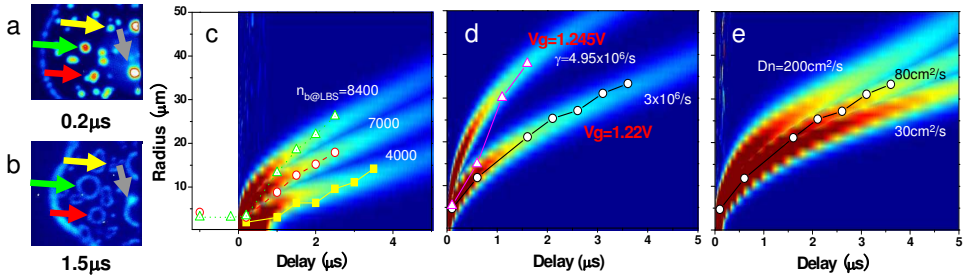

Figure 4.7: LBS ring kinetics. (a,b) Images of emission of indirect excitons at time delays $t = 0.2$ and 1.5 μs after the laser pulse end. (c) Measured kinetics of the LBS ring radius for three different LBS marked in (a,b) by the arrows at V_g =1.235V and P_{ex}=1.82mW (points). An LBS with a stronger emission (a) is characterized by a faster LBS ring expansion (c). The simulated kinetics for different $n_{b@LBS} = 4000, 7000$ and 8400 at $p_b = 10$ and $n_{b@other} = 0.05$ are presented by false color images. (d) Measured kinetics of the LBS ring radius [for LBS marked by gray arrow in (a)] for different $V_g = 1.22$ and 1.245 V at $P_{ex} = 0.76$ mW (points). The simulated kinetics for different $\gamma = 3$ and 4.95×10^6 s^{-1} are presented by false color images. $n_{b@LBS} = 12600$ and $n_{b@other} = 0.05$ in simulations in (d). $D_n = 80$ cm^2/s, $D_p = 26$ cm^2/s, and $w = 64$ in the simulations in (c,d).(e) Comparison of simulated kinetics for different $D_n = 30, 80$ and 200 cm^2/s with the rest of the parameters same as in (d). $D_n = 80$ cm^2/s results to a better fit of the experimental kinetics for $V_g = 1.22$ V in (d). The size of LBS is 0.26 μm in all simulations in (c-e).[83]

Chapter 5

Macroscopically ordered exciton state (MOES)

5.1 Introduction

Spontaneous macroscopic ordering is a general phenomenon in pattern formation. For instance, periodic 1D patterns are observed in a variety of both quantum and classical systems. The examples include the soliton trains in atom Bose-Einstein condensates (BEC) [74], Taylor vortices in liquids [77], Turing instabilities in reaction-diffusion systems [18] and bacteria colonies [78], and gravitational instabilities in cosmological systems [19]. All of these ordered states originate from an instability, which is generated by a positive feedback to density modulation. The mechanism of the positive feedback is specific for each system. A particular mechanism of the positive feedback, which is responsible for the soliton train formation [74] and gravitational instability [19], is an attractive interaction: In the experiments on atom BEC, the stripe of atomic BEC was homogeneous in the case of repulsive interaction and, conversely, was fragmented to the periodic soliton train in the case of attractive interaction due to the modulational instability [74]; Gravitational instability results

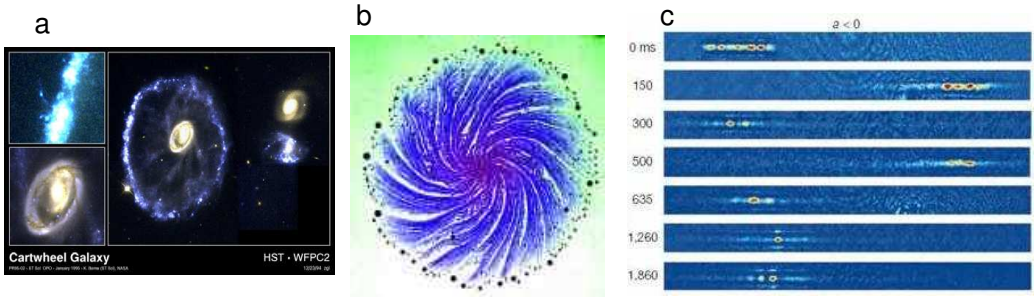

Figure 5.1: Examples of fragmentation in other systems. (a) gravitational instabilities in cosmological systems [19], (b)Turing instabilities in bacteria colonies [78], (c) soliton trains in atom Bose-Einstein condensates (BEC) [74]

in the fragmentation of gaseous slabs and filaments to a periodic array of high-density clumps that is a step towards the formation of stars [19].

5.2 Interaction

In this section, we address an issue of interaction in MOES. If the interaction appears to be attractive then it could naturally lead to the density modulation in the exciton ring as attractive interaction leads to the density modulation in a variety of systems, which spread from cold atoms [74] to cosmological systems [19]. Several theoretical models, which are based on the assumption of attractive interaction, have been suggested to explain the MOES. According to these models, attractive interaction may originate from Van der Waals and exchange interactions between the indirect excitons [75, 76], from plasmon or phonon wind [51], or from the in-plane exciton dipole alignment [15].

However, the CQW geometry [17] is engineered so that the interaction between excitons is repulsive: Indirect excitons, formed from electrons and holes confined to different QWs, behave as dipoles oriented perpendicular to the quantum well plane

(Fig. 1a) and an exciton or electron-hole density increase causes an enhancement of energy [87, 89, 55]. The repulsive character of interaction was evident in earlier experiments as a positive line shift with increasing density [10]. The objective of this study is to verify if the interaction remains repulsive at low temperatures in the regime of the MOES or changes sign and becomes attractive thus naturally leading to the density modulation, i.e. to the MOES formation.

The experimental results presented in this section show that the interaction is repulsive in the regime of MOES. Therefore, the interaction cannot be responsible for the MOES formation and, on the contrary, acts against the density modulation. This finding eliminates attractive interaction as a possible mechanism for the MOES formation.

The spatial $x - y$ photoluminescence (PL) pattern was measured by a liquid-nitrogen-cooled CCD camera after spectral selection by an 800 ± 5 nm interference filter chosen to match the indirect exciton energy. As a result, the low-energy bulk emission, higher-energy direct exciton emission, and scattered laser light were effectively removed and the indirect exciton PL emission intensity was directly visualized in $x - y$ spatial coordinates. The scheme of the experiment is shown in Fig. 5.2b. Fig. 5.2d shows the indirect exciton PL pattern at $T = 1.6$ K and excitation power $P_{ex} = 0.25$ mW. The laser excitation spot is in the center of the image. The external exciton ring, LBS, and MOES are clearly seen in the image.

In addition, we measured the exciton PL energy profiles along the ring using the experimental scheme shown in Fig. 5.2c: a segment of the ring was projected on the spectrometer slit and the image was dispersed by a spectrometer without spectral selection by an interference filter. The selected part of the external ring was parallel to the spectrometer entrance slit and the slit width (0.1mm) was small enough to get a high spectral resolution (0.1nm). The spatial resolution in the x-direction was 2μm. The measured images of the PL signal in the *energy-coordinate* plane are presented in Fig. 5.2e for different temperatures.

Fig. 5.2e shows the indirect exciton energy profile along the selected part of the ring. The black lines show variation of the average PL energy $E_{PL}(x) = \frac{\int\int E(x,y,\lambda)I(x,y,\lambda)dyd\lambda}{\int\int I(x,y,\lambda)dyd\lambda}$ of the indirect excitons along the circumference of the ring. The indirect exciton PL intensity modulation increases drastically with reducing temperature, which indicates formation of the MOES. This is consistent with the earlier studies [13, 16]. The measurements presented in Fig. 5.2e show that the increase of PL intensity modulation with reducing temperature is accompanied by the increase of PL energy modulation.

The variations of the spectrally integrated PL intensity $I_{PL}(x) = \int\int I(x,y,\lambda)dyd\lambda$ and average energy $E_{PL}(x)$ of the indirect excitons along the circumference of the ring are shown in Fig. 5.3b. The PL energy varies in concert with the intensity along the circumference of the ring, with the largest energy found in the brightest regions. The corresponding spectra in a bead center and in a valley between two beads are shown on Fig. 5.3a. The indirect exciton PL intensity and energy are higher in the bead center. These experimental results show that the MOES is characterized by the repulsive interaction and is not driven by the attractive interaction.

We have also addressed an issue whether formation of MOES lowers the total energy of the exciton system in the ring. For this purpose, we measured the spatially average energy of indirect excitons in the external ring $E_{avg} = \frac{\int\int\int E(x,y,\lambda)I(x,y,\lambda)dxdyd\lambda}{\int\int\int I(x,y,\lambda)dxdyd\lambda}$ as a function of temperature, see Fig. 5.4b. The contrast of the exciton density modulation along the ring with length L is presented by the height of the peak of its Fourier transform $I(k) = \frac{1}{\int_0^L I(l)dl}\int_0^L I(l)e^{-ikl}dl$ at $k = \frac{2\pi}{\lambda_{MOES}}$, which corresponds to the modulation wavelength λ_{MOES}. It is shown in Fig. 5.4a for comparison. Fig. 5.4b shows that the average energy of the indirect excitons in the ring depends non monotonically on temperature with a transition around $T_{tr} \sim 4$ K: with reducing temperature, the energy reduces until T_{tr} and increases below T_{tr}. Note that the average indirect exciton PL energy exhibits a transition simultaneously with the MOES onset at ca. 4 K, compare Fig. 5.4a and Fig. 5.4b.

Fig. 5.4 indicates that MOES formation is accompanied by an increase of the total energy of excitons in the ring and, therefore, the density modulation is not caused by lowering the total energy of the system. This confirms that the MOES formation is not driven by the attraction interaction. Note that such a behavior is not unusual for pattern formations in quasi-equilibrium systems and, in particular, is consistent with a model [50] showing that a spatially modulated exciton state can result from a nonlinear density dependence of the exciton formation rate in the ring. Next section, we will briefly review that model.

5.3 Model based on stimulated scattering

This model proposed in [50] explained MOES as a result of Turing instability. Turing instability is due to balance between diffusion and reaction. Indirect exciton repels each other, try to diffuse outwards and keep the density even. On the contrary, reaction mechanism try to increase the exciton density in certain places while decrease the density elsewhere. MOES is a low temperature effect, the critical temperature is close to de Broglie temperature where exciton gas becomes quantum. So the model proposes the reaction mechanism is stimulated scattering due to quantum degeneracy.

This model starts from the transportation equations in last chapter:

$$\begin{cases} \partial_t n = D_{\mathrm{e}} \nabla^2 n - wnp + J_{\mathrm{e}}, \\ \partial_t p = D_{\mathrm{h}} \nabla^2 p - wnp + J_{\mathrm{h}} \\ \partial_t n_{\mathrm{x}} = D_{\mathrm{x}} \nabla^2 n_{\mathrm{x}} + wnp - \gamma_x n_{\mathrm{x}} \end{cases} \tag{5.1}$$

In quantum degeneracy region, formation rate of exciton w will be increased by factor $f = 1 + N_E^{eq}$, where N_E^{eq} denotes the occupation of exciton states. In low temperature and thermal equilibrium, reverse process of dissociation can be ignored, because the binding energy $5meV$ is way higher than $k_B T$. This f factor can be

expressed:

$f = e^u$, $u \equiv \frac{n_x}{n_0(T)}$, $n_0(T) = \frac{2gm_x k_B T}{\pi\hbar^2}$

It is shown that when $u > u_c = (1 + r^{1/2})^2$, instability arises in the system. The spatial modulation wavelength is $\lambda_c \sim l^{1/3} l_x^{2/3}$. Here $r = D_x(D_e^{-1} + D_h^{-1})\bar{n}_x/\bar{n}_e$, $\bar{n}_x = J/\gamma_x$, $\bar{n}_{e,h} = J/w(\bar{n}_x)^{1/2}$, $J = J_e = J_h$. [50]

The simple physics picture of this instability is: a local fluctuation in the exciton density leads to an increase in the stimulated exciton formation rate. The associated depletion of the local carrier concentration causes neighboring carriers to transport towards the point of fluctuation presenting a mechanism of positive feedback.

5.4 Commensurability

Commensurability is a common phenomenon in waves. It happens when a wave is confined in a limited region or in a closed loop. When there is a integer number of wavelength between boundaries, the wave is stable, when there is non-integer number of wavelength between boundaries the wave is instable. Spatial ordering with commensurability is a phenomenon not only existed in quantum world. Harmonic modes in guitar's strings or in the pipe of a flute are examples in classical world. A wave can form a standing wave by interference with itself, and this is one of the ideas which lead to the born of quantum mechanics.

Commensurability in low temperature usually relate to interesting physics, e.g. periodical modulation of electrons in transition metal-chalcogenides (charge density wave) leads to research on anisotropic fermi surface, vortex lattice in cold atom clouds relates to superfluidity [2].

MOES in external ring is a density wave. In this section, we will present the study on its fluctuation and commensurability.

The spatial $x - y$ photoluminescence (PL) pattern was measured by a liquid-nitrogen-cooled CCD camera or video camera after spectral selection by an 800 ± 5

nm interference filter chosen to match the indirect exciton energy. As a result, the low-energy bulk emission, higher-energy direct exciton emission, and scattered laser light were effectively removed and the indirect exciton PL emission intensity was directly visualized in $x - y$ spatial coordinates.

The first question we study is if this density wave is spontaneous. Traps with certain period on the surface of the sample could result in a periodical density modulation. In order to verify this, we keep the density wave in the same place in the sample and try to see if we can change its wavelength. We can make this by tuning both the gate voltage and laser excitation power, because from previous chapter, we know changing both laser power and gate voltage in the same ratio will keep the ring in the same position. Exciton density along the ring will change. In Fig. 5.6a-b, we show PL images and profile along the ring with two sets of parameters, $V_g = 1.26V$, $W_{laser} = 1.12mW$ (Fig. 5.6a) and $V_g = 1.13V$, $W_{laser} = 0.028mW$ (Fig. 5.6b). With laser power different by 40 times, external ring is in the same sample position, while the wavelength of density wave is different by 3 times. In Fig. 5.6c, we plot the relation between wavelength of MOES and both gate voltage and excitation laser power. The wavelength changes with these parameters up to several times. So the density wave cannot form due to the local trappings in the sample. This can also be proved from Fig. 5.6d. There peak positions of the modulation are plotted versus peak numbers at both low and high exciton densities. They are in linear in both cases, that means the periodicity is not fixed by local potential wells in the sample. That means the phase of this macroscopic exciton density wave is spontaneous.

Fig. 5.7a shows a real space PL image of the sample. We can see external ring passes through several LBSs on the sample. LBS is electron source in the sample, so it attracts the hole flow around it. Around one LBS, there is always a electron-hole interface, thus an exciton ring. So those LBSs pin down the phase of density wave. With all physical parameters fixed, the density wave fluctuates in between those LBSs. The fluctuation frequency is in the scale of 10Hz. To study this fluctuation

we use a video camera to take real time movies with all physical parameters fixed. The frame rate is 30frames/s. Fig. 5.7b shows two images extracted from it. The images show the fluctuation in one part of the ring in Fig. 5.7a. Bead 2 shifts its position from one frame to the other. We track the fluctuation by measuring the fluctuation of intensity in two fixed position in the sample, one is in the density wave and the other is next to a LBS, both positions are marked by cross in the image. Fig. 5.7d shows PL intensity changing with time. The two positions have the similar PL average intensity but the fluctuation in the density wave is much stronger that that of the one next to a LBS. In Fig. 5.7c we show the normalized standard deviation of PL intensity in 900 frames for the whole area, yellow color indicates high deviation thus high fluctuation, and dark color indicates low deviation thus low fluctuation. From that, it is obvious, LBS is much more stable than density wave.

Another way to measure stability of density wave is by tracking the bead position versus time. In Fig. 5.7e, we measure the position of bead 1 and 2 marked in Fig. 5.7b in time. It shows the phase of the macroscopic exciton density wave (i.e. the MOES) is fixed at the LBS, while the density wave in between two LBS is fluctuating.

The amplitude of fluctuation in between LBS is not uniform. It is much stronger in the region where the density wave changes from one period to another. We define filling number $\nu = L/\lambda$ as a measure of periodicity, L is the distance between two LBSs that are at both ends of density wave, λ is the wavelength. ν is changed by changing exciton density while keeping the ring in the same position in the sample. We use gate voltage as a measure of the exciton density.

We select a region in Fig. 5.8a and observe the fluctuation when density wave filling number changes from $\nu = 8$ to $\nu = 6$. Fluctuation is measured by monitoring PL fluctuation in a fixed point in time (marked by the cross in Fig. 5.8a). Fig. 5.8b shows the fluctuation with $\nu = 8$, $\nu = 6$ and some value in between. Another way to measure fluctuation, we track the positions of beads in time, the results are shown in Fig. 5.8c. From both ways, we can see fluctuation is low when filling number

is integer ($\nu = 8$, $\nu = 6$), fluctuation is much stronger when filling number is not integer.

To get a quantitative analyze, we use second order correlation function of the density wave as a quantitative measure of stability of wave. We choose a segment of the ring between LBS A and LBS B, shown in (Fig. 5.9b). We measure the second order spatial correlation function $g^{(2)}(R) = \frac{\langle I(r)I(r+R)\rangle}{\langle I(r)\rangle^2}$ in the PL profile along the ring. The average is done for 27 seconds movie (30 frames per second). Fig. 5.9a shows two curves of $g^{(2)}(R)$ with different filling numbers, i.e. exciton densities. The period of modulation in $g^{(2)}(R)$ corresponds to the period of the exciton density wave. Because fluctuation of the phase reduce the modulation in $g^{(2)}(R)$, the amplitude of the modulation shows how stable the wave keeps. So we use the standard deviation of $g^{(2)}(R)$ as the qualitative measure of the stability of the exciton density wave. In Fig. 5.9c, we plot the standard deviation of $g^{(2)}(R)$ versus gate voltage, i.e. exciton density. It shows that the wave is stable when there is an integer number of beads in the ring segment in between the LBS(A and B), e.g. the $\nu = 5$ and $\nu = 6$ in the plot. And it is not stable when the filling number is non-integer. This shows commensurability in this exciton density wave.

From LBS A to LBS B, there are hundreds of thousands excitons. This exciton density wave is a collective state of many excitons. This commensurability may relate to quantum degeneracy.

5.5 Acknowledgements

The text of chapter 5, in part, is a reprint of the material as it appears in Sen Yang, A.V. Mintsev, A.T. Hammack, L.V. Butov, and A.C. Gossard, *The Role of Interaction in the Formation of Macroscopic Ordering in Exciton Rings*, Phys. Rev. B **75**, 033311, © 2007 The American Physical Society, where the dissertation author was the first author. The co-authors in these publications directed, supervised, and

co-worked on the research which forms the basis of this chapter.

The text of chapter 5, in part, is a reprint of the material as it appears in Sen Yang, L.V. Butov, L.S. Levitov, B.D. Simons, and A.C. Gossard, *Commensurability of macroscopic exciton density wave*, where the dissertation author was the first author. The co-authors in these publications directed, supervised, and co-worked on the research which forms the basis of this chapter.

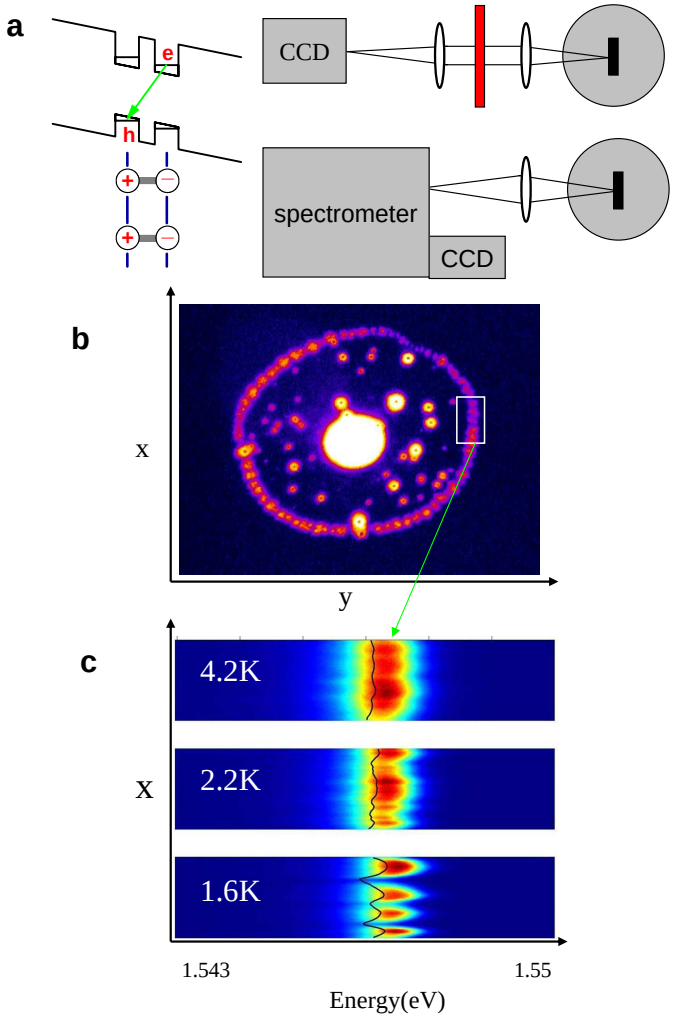

Figure 5.2: (a) Energy band diagram of the CQW structure; e is electron, h - hole. Scheme of the experimental setup for imaging PL signals in $x-y$ coordinates (b) and $E-x$ coordinates (c). (d) PL image of indirect excitons in $x-y$ coordinates at $T = 1.6$ K. The area of view is $365 \times 275\,\mu$m. (e) Spectrally resolved PL image of indirect excitons in $E-x$ coordinates for the ring segment, which is marked by a rectangle in (d), at $T = 1.6, 2.2$, and 4.2 K. The length of view (vertical axis) is $50\,\mu$m for each image. The black lines show variation of the PL energy of the indirect excitons along the circumference of the ring. $V_g = 1.211$ V and $P_{ex} = 0.25$ mW for the data.[82]

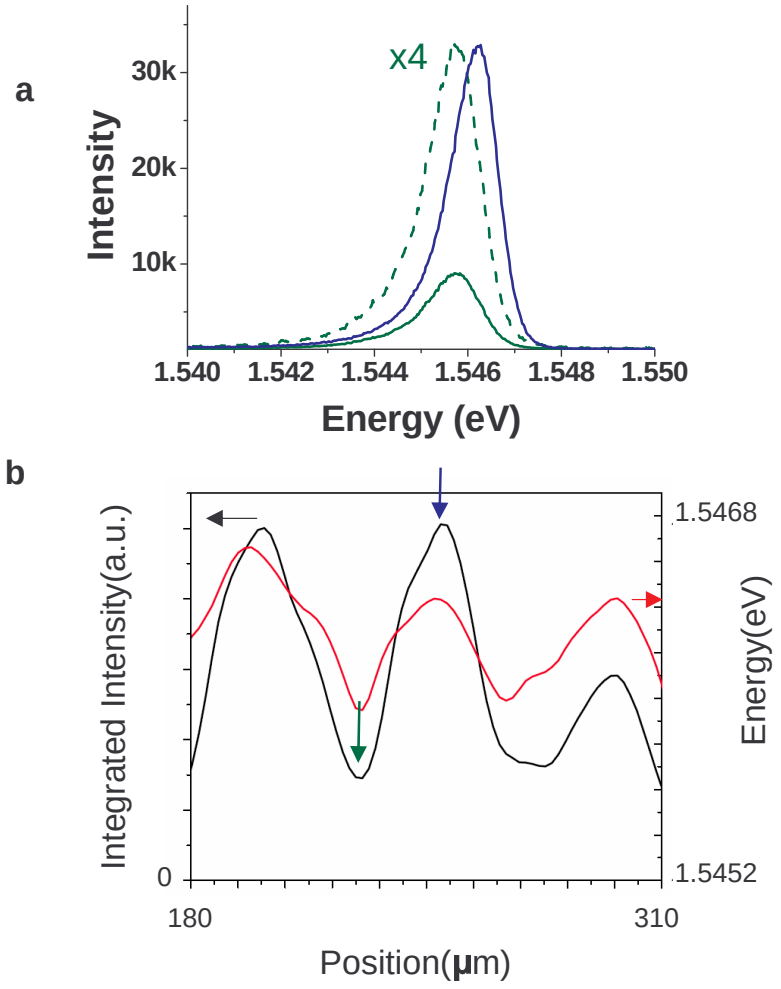

Figure 5.3: (a) The indirect exciton PL spectrum in the bead center (bold blue line) and in between two beads (thin green line, dashed green line shows the same spectrum multiplied by a factor of 4 for comparison). (b) Variation of the PL energy and intensity of the indirect excitons along the circumference of the ring. $T = 1.6$ K, $V_g = 1.30$ V and $P_{ex} = 8.6$mW for the data. The indirect exciton energy increases with increasing density indicating repulsive interaction in the regime of MOES.[82]

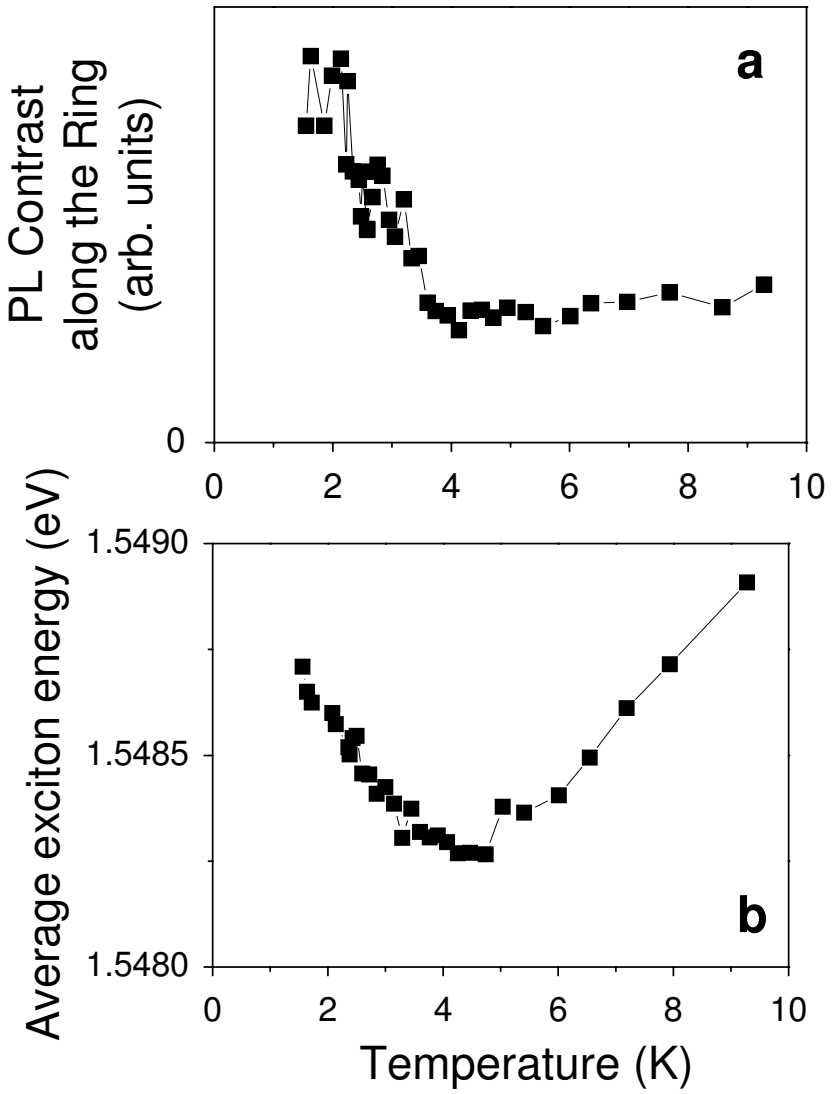

Figure 5.4: (a) Exciton density Fourier transform peak height at the fragmentation period and (b) spatially averaged energy of indirect excitons in the ring vs. temperature. $V_g = 1.15V$ and $P_{ex} = 118\mu$W for the data.[82]

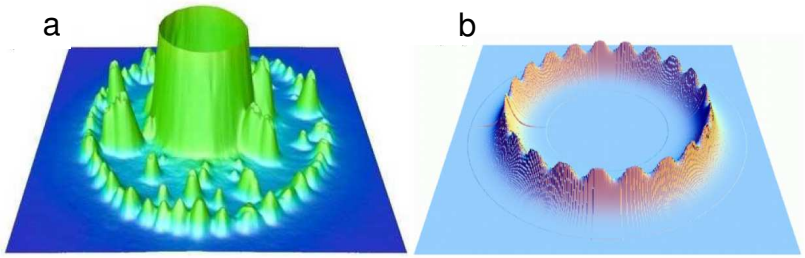

Figure 5.5: Model of stimulated scattering (a) 3D image of real space PL, (b) results from simulation. [50]

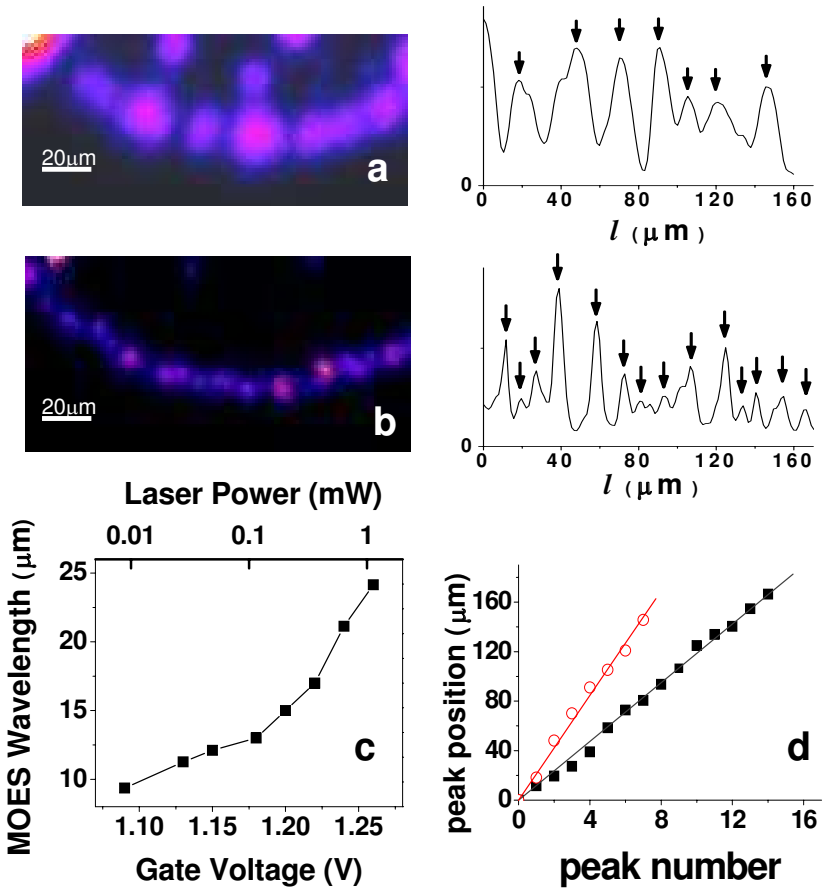

Figure 5.6: (a),(b) left column: PL image of indirect exciton external ring in $x - y$ coordinates at $T = 1.6$ K. right column: PL profile along the ring. (a), the gate voltage is 1.26 V and excitation laser power 1.12 mW. (b) the gate voltage is 1.13 V and excitation laser power 0.028 mW. (c) the MOES wavelength vs. gate voltage and excitation laser power with fixed ring position. (d) the PL peak positions in (a) (red circle) and (b) (black dot). [84]

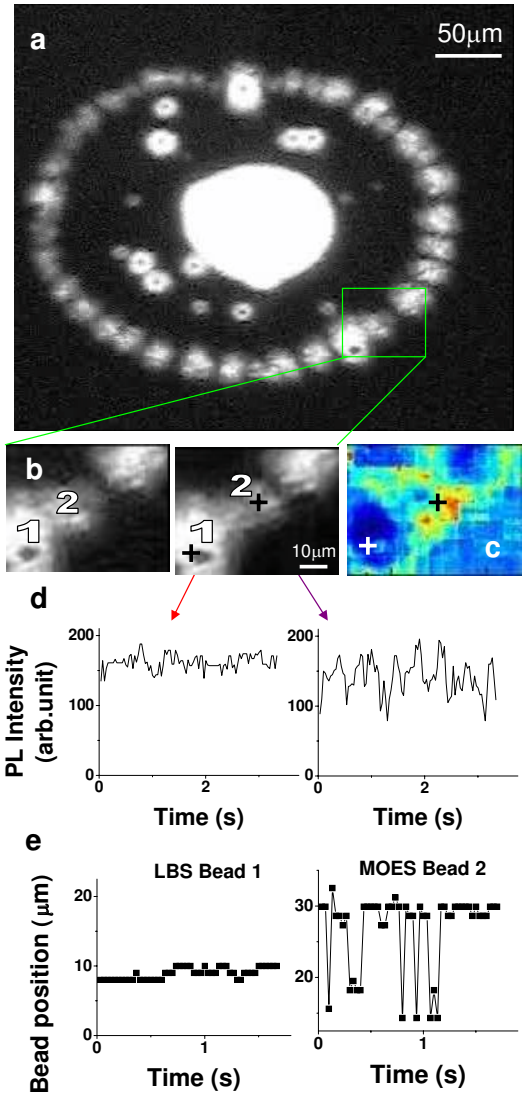

Figure 5.7: (a), (b) PL images of the indirect exciton pattern extracted from a real time movie. The position of the bead fluctuates with time. Two images in (b) are from the same position and same physical parameters but different time. (c) Standard deviation of indirect excitons PL intensity, yellow color indicates high fluctuation regions, and dark color indicates low fluctuation regions. (d) PL intensity vs. time in fixed points marked by a cross in the images. (e) bead position vs. time for localized bright spot (LBS) bead and MOES bead. All the data were taken with gate voltage $V_g = 1.217$ V, at $T = 1.6$ K. [84]

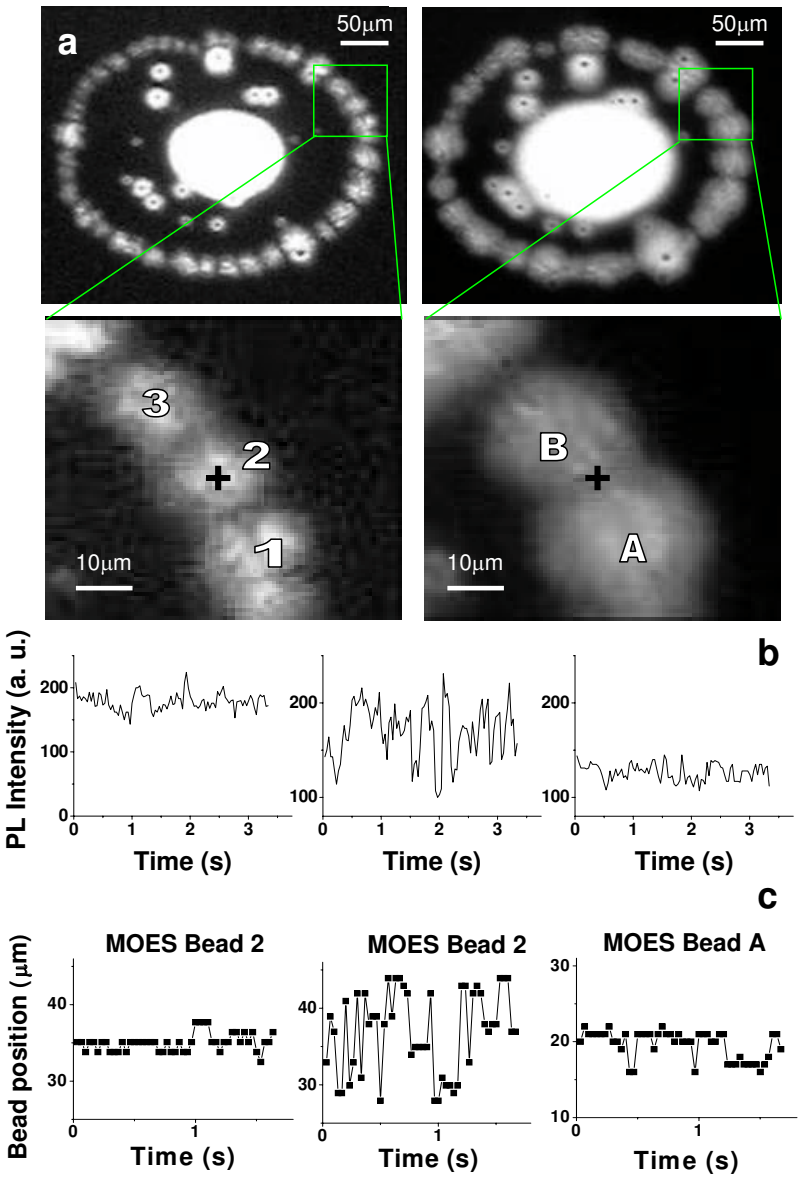

Figure 5.8: (a) PL image of indirect exciton ring with different filling numbers in selected region. Both filling numbers $\nu = L/\lambda$ are integers. $\nu = 8$ (left) and $\nu = 6$ (right). (b) PL intensity vs. time with integer filling numbers (left and right) and non-integer (middle) in fixed points marked by a cross in the images. (c) bead position vs. time in the same condition of (b). The gate voltage is 1.219 V for $\nu = 8$ (left), 1.233 V for ν is non-integer (middle) and 1.263 V for $\nu = 6$ (right). The temperature is $T = 1.6$ K. [84]

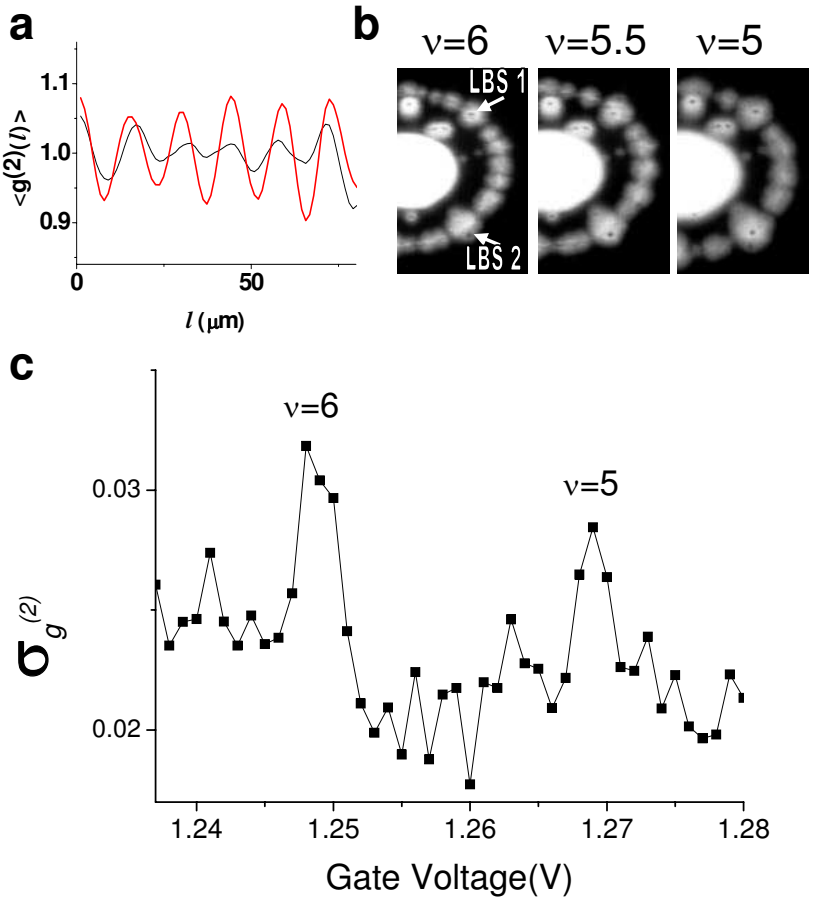

Figure 5.9: (a) The second order correlation function of exciton density wave $g^{(2)}(l) = \frac{\langle I(l')I(l'+l)\rangle}{\langle I(l')\rangle^2}$ was calculated from the profile along the segment of the ring between LBS 1 and 2 (shown in (b)), then averaged for 800 frames in 27 second movie. The filling numbers are $\nu = 7$ (red) and ν is about 6.5 (black). (b) PL image of indirect excitons averaged for 800 frames for three filling numbers. (c) standard deviation of $\langle g^{(2)}\rangle$ as a function of gate voltage. All data were taken at $T = 1.6$ K. [84]

Chapter 6

Coherence

6.1 Introduction

Coherence of excitons in quantum wells attracts considerable interest. It has been intensively studied by four-wave-mixing [20], coherent control [57], and interferometric and speckle analysis of resonant Rayleigh scattering [7, 48, 30]. In all these experiments, exciton coherence was induced by a resonant laser excitation and was lost within a few ps after the excitation pulse due to exciton-exciton and exciton-phonon collisions and due to inhomogeneous broadening by disorder.

Another fundamentally interesting type of coherence is spontaneous coherence (not driven by the laser excitation). Studies of spontaneous coherence of excitons require implementation of cold exciton gases, see below. This can be achieved with indirect excitons in coupled quantum wells (CQW) [17]. Taking advantage of their long lifetime and high cooling rate, one can realize a gas of indirect excitons with temperature well below 1 K and density in excess of $10^{10}\,\mathrm{cm}^{-2}$ [17]. For comparison, the crossover from classical to quantum gas occurs at $T_{\mathrm{dB}} = 2\pi\hbar^2 n/(mgk_{\mathrm{B}})$ and $T_{\mathrm{dB}} \approx 3\,\mathrm{K}$ for the exciton density per spin state $n/g = 10^{10}\mathrm{cm}^{-2}$ (exciton mass $m = 0.22m_0$, and spin degeneracy $g = 4$ for the GaAs/AlGaAs QWs [17]). Note

that at this density $na_B^2 \sim 0.1$ and, therefore, excitons are interacting hydrogen-like Bose particles [43] ($a_B \approx 20$ nm is the exciton Bohr radius [23]).

Spontaneous coherence can be experimentally studied using nonresonant laser excitation so that coherence is not driven by the laser. However, nonresonant excitation may lead to strong heating of the excitons in the excitation spot [12]. Therefore, in this chapter we study coherence in the external exciton rings [13], which form far away from the excitation spot (Fig. 6.1c), at the border between the electron- and hole-rich regions [16, 66]. The external ring of indirect excitons in CQW is the region where the exciton gas is cold: The excitons in the ring are formed from well-thermalized carriers and their temperature essentially reaches that of the lattice. The cold exciton gas in the external ring can form a macroscopically ordered exciton state (MOES) — an array of beads with spatial order on a macroscopic length [13]. The MOES appears abruptly along the ring at T below a few Kelvin.

6.2 Measurement

Our experimental setup (Fig. 6.1b) is a variant of Mach-Zehnder (MZ) interferometry with new ingredients. First, we added spatial resolution by collecting the light only from a selected area of size $D/M_1 = 2$–$10\,\mu$m in the middle of a MOES bead (Fig. 6.1c). This was done by placing a pinhole of diameter $D = 10$–$50\,\mu$m at the intermediate image plane of magnification $M_1 = 5$. Second, we added the frequency resolution by dispersing the output of the MZ interferometer with a grating spectrometer. (The image was further magnified by the factor $M_2 \approx 2$ after the pinhole.) The output of the spectrometer was imaged by a nitrogen cooled CCD (Fig. 6.1b). The MZ delay length δl was controlled by a piezo-mechanical translation stage. The PL pattern of the indirect excitons (Fig. 6.1c) was also imaged with the pinhole removed and the image filtered at the indirect exciton energy (dashed path in Fig. 6.1b). The excitation was supplied by HeNe laser at 633 nm (the laser

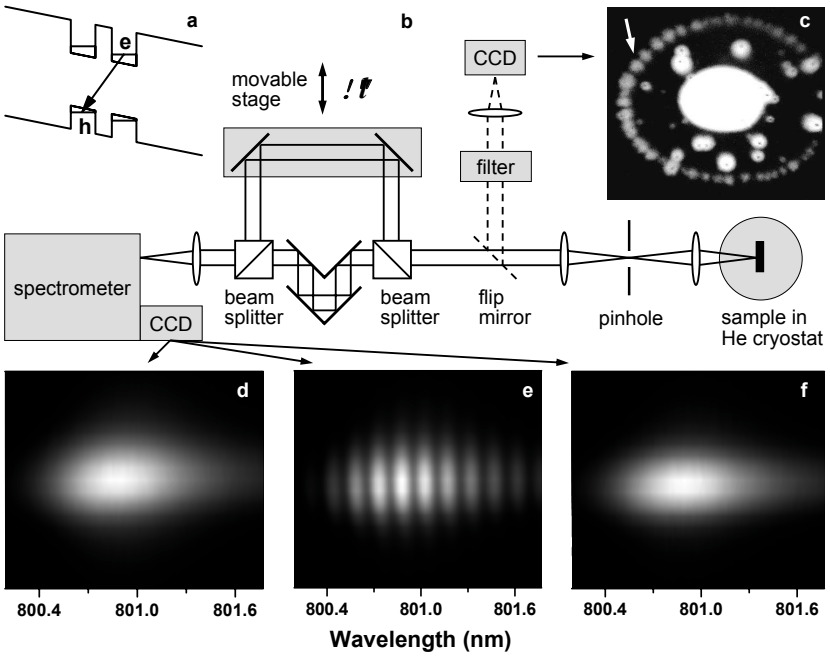

Figure 6.1: (a) The CQW band diagram. (b) Scheme of MZ interferometer with spatial and spectral resolution. (c) The pattern of indirect exciton PL. The area of view is $280 \times 250\,\mu$m. Spectra for the left (d), right (f), and both (e) arms of the MZ interferometer. The light was selected from the center of the arrow-marked MOES bead. The length of view (vertical axis) is $25\,\mu$m. $T = 1.6$ K, $V_g = 1.24$ V, $D = 25\,\mu$m, $\delta l = 4.2$ mm, and $P_{ex} = 0.7$ mW for all the data. [81]

excitation spot with FWHM 7 μm is in the center of the exciton ring, Fig. 6.1c). The excitation was 400 meV above the indirect exciton energy and well separated in space; therefore, no laser-driven coherence was possible in the experiment.

An example of the measured interference pattern is shown in Fig. 6.1e. The light was collected from the center of a bead shown in Fig. 1c by the arrow. (While all interference profiles in the paper refer to this spot, similar profiles were measured from other spots on the ring.) The modulation period $\delta\lambda$ of the CCD signal I was deduced from the locations of the satellite peaks of Fourier transform of I,

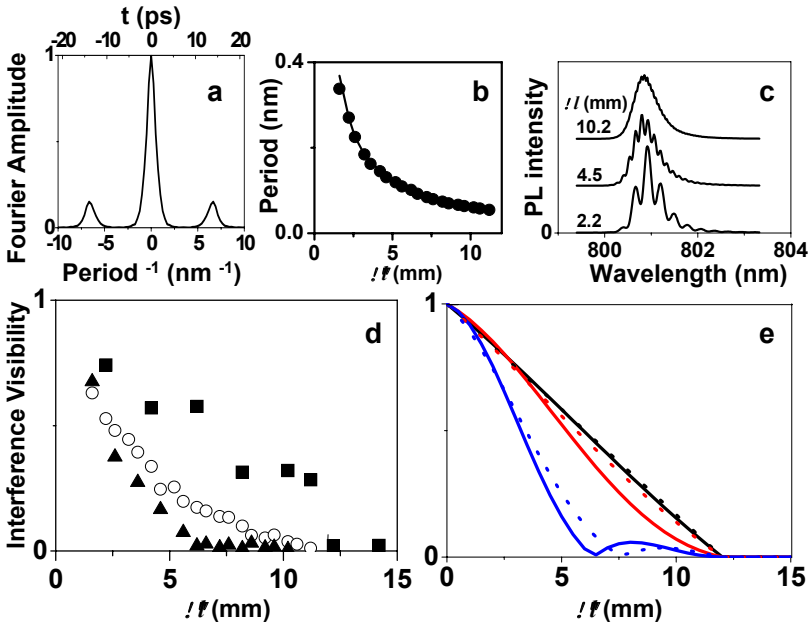

Figure 6.2: (a) The Fourier transforms of the CCD signal for $D = 50\,\mu$m and $\delta l = 4.2$ mm. (b) Period of the interference fringes vs δl. Solid line: fit to $\delta\lambda = \lambda^2/\delta l$. (c) Interference profiles for $D = 50\,\mu$m and $\delta l = 2.2, 4.5$, and 10.2 mm. (d) Measured and (e) calculated visibility of the interference fringes vs δl for $D = 50$ (triangles, blue), 25 (circles, red), $10\,\mu$m (squares, black), and $M_2 = 1.7$. Solid and dotted lines in (e) correspond to the Eqs. (6.18) and (6.19), respectively. $T = 1.6$ K, $V_g = 1.24$ V, $P_{ex} = 0.7$ mW for all the data. [81]

Fig. 6.2a. It was found to obey the expected dependence $\delta\lambda = \lambda^2/\delta l$ (see Fig. 6.2b and below). To quantify the amplitude of the modulations we computed their visibility factor $V = (I_{\max} - I_{\min})/(I_{\max} + I_{\min})$ using a method based on the Fourier analysis [Eq. (6.2)]. The visibility factor was examined for a set of δl and T.

The main experimental result is presented in Fig. 6.3c: Visibility of the interference fringes sharply increases at temperatures below a few Kelvin. This contrasts with the T-independent V of the direct exciton emission measured at the excitation spot center at $T = 2$–10 K.

Let us proceed to the data analysis. Recall that for a classical source with a Lorentzian emission lineshape, the first-order coherence function [Eq. (6.14)] at the coincident points is given by $g(t, \mathbf{r} = 0) = \exp(-t/\tau_c)$, where τ_c is the inverse linewidth. By analogy, we assume the r-dependence in the form $g(t, \mathbf{r}) = g(t, 0) \exp(-r/\xi)$, where ξ is the coherence length. Our goal is to deduce ξ from the contrast of the periodic modulations in the CCD image, Fig. 1e. Consider the central row of that image. Let x be a coordinate along this row and let x_0 be the position of the diffraction maximum for the central frequency of the emission line $\omega_0 = 2\pi c/\lambda_0$. Due to small width of this line, it is permissible to work with small deviations $\delta x = x - x_0$, $\delta\omega = \omega - \omega_0$, and $\delta\lambda = \lambda - \lambda_0$. (Thus, the horizontal axes in Figs. 1d–f and 2c are labelled by the "wavelength" λ using the conversion formula $\delta\lambda/\lambda_0 = \delta x/x_0$.)

As mentioned above, the Fourier transform

$$\tilde{I}(t) = \int dx \exp\left(-it\omega_0 x/x_0\right) I(x) \tag{6.1}$$

is found to possess three peaks: the main one, at $t = 0$, and two satellites, Fig. 2a. We will show that these satellites occur at $|t| = \tau = \delta l/c$. We will also explain the fact that the shapes of the three peaks in Fig. 2a are nearly identical. Because of the latter the amplitude of the oscillations in $I(x)$ is fully characterized by the relative height of the main and the satellite peaks. Therefore, we define the visibility factor by

$$V = 2|\tilde{I}(\tau)|/\tilde{I}(0). \tag{6.2}$$

Next, we note that the central row of the CCD image in Fig. 1d–f is generated by the sources situated on the pinhole's diameter. Thus, instead of two-dimensional vector $\mathbf{r}$, it suffices to use the linear coordinate y along the magnified image of such a diameter, of length $D_s = M_2 D$, at the spectrometer input slit.

The intensity of the CCD image averaged over a large time T_{im} is a result of interaction of the original PL signal $E(t, y)$ with two linear devices, the MZ inter-

ferometer and the spectrometer. It is convenient to do the calculation of their combined effect in the frequency domain. We define the Fourier amplitudes $\tilde{E}(\omega_j, y) = \langle E(t, y) \exp(i\omega_j t) \rangle$, for a set of frequencies $\omega_j = 2\pi j / T_{im}$. A straightforward derivation leads to

$$I(x) = \int_{-D_s/2}^{D_s/2} \int_{-D_s/2}^{D_s/2} dy_1 dy_2 \sum_{\omega_j} |1 + \exp(i\omega\tau)|^2 \tilde{E}(\omega_j, y_1) \tilde{E}(-\omega_j, y_2) f_s(x, \omega_j, y_1) f_s(x, \omega_j, y_2), \tag{6.3}$$

where

$$f_s(x, \omega, y) = \frac{\sin(\pi N z)}{\pi z}, \quad z = \frac{\delta\omega - By}{\omega_0} + \frac{\delta x}{x_0} \tag{6.4}$$

is the response function of the spectrometer, which is obtained from the standard formula for the diffraction grating of N grooves by expansion in $\delta\omega$ and δx. Parameter B is determined by the linear dispersion of the spectrometer $A = 1.55\,\mathrm{nm/mm}$, via the relation $B = 2\pi c A / \lambda_0^2$. After algebraic manipulations with Eqs. (6.14), (6.1), (6.3), and (6.4), we get the following expression for the case of practical interest, $|t| < 2\pi N / \omega_0$:

$$\tilde{I}(t) \propto \int_0^{D_s} \frac{dy}{yt} \sin\left[\frac{1}{2}(D_s - |y|)Bt\right] \sin\left[\left(\frac{2\pi N}{\omega_0} - |t|\right)\frac{B}{2} y\right] \times \left[g(t, y) + \frac{1}{2} g(t - \tau, y) + \frac{1}{2} g(t + \tau, y)\right]. \tag{6.5}$$

The three-peak structure of $\tilde{I}(t)$ described above stems from the three terms on the last line of Eq. (6.5). The width of each peak is exactly the coherence time τ_c. The peaks are well separated at $\tau \gg \tau_c$ and their shape is nearly identical if τ_c is sufficiently small. The heights $\tilde{I}(0)$ and $\tilde{I}(\tau)$ of the peaks are determined by the first

and the second terms on the last line of Eq. (6.5), and so

$$V = \frac{\theta(1-\Delta)\int\limits_0^1 z^{-1}\sin[F(1-\Delta)z]\sin[F\Delta(1-z)]\tilde{g}(z)dz}{F\Delta\int\limits_0^1 z^{-1}\sin(Fz)(1-z)\tilde{g}(z)dz},$$
$$F \equiv \frac{\pi N A D_s}{\lambda_0}, \quad \tilde{g}(z) \equiv g\left(0, \frac{zD}{M_1}\right), \quad \Delta \equiv \frac{\delta l}{N\lambda_0}. \tag{6.6}$$

To understand the implications of this formula consider first the case of an infinite diffraction grating, $N \to \infty$. Here $\Delta \to 0$, $F \to \infty$ but the product $F\Delta = \pi A D_s \delta l/\lambda_0^2$ remains finite. For the visibility we get

$$V = |\sin(F\Delta)|/F\Delta, \tag{6.7}$$

so that function $V(\delta l)$ has a periodic sequence of nodes at $\delta l = n\lambda_0^2/(AD_s)$, where $n = 1, 2, \ldots$, and does not depend on ξ. Equation (6.7) is reminiscent of the Fraunhofer formula for diffraction through a slit of width D_s.

In reality N is large but finite. In this case the dependence on ξ does show up. Thus, for $M\xi \ll \lambda_0/AN$, where $M = M_1M_2$, Eq. (6.18) reduces to

$$V = \frac{1-\Delta}{f\Delta}|\sin(f\Delta)|, \quad f = \frac{\pi N A}{\lambda_0}(M_2 D - M\xi). \tag{6.8}$$

To understand the origin of Eqs. (6.7) and (6.19) consider the signal at the center of the CCD image, at point x_0. It is created by interference between all pairs of elementary input sources whose coordinates $y_1 = y + \delta y$ and $y_2 = y - \delta y$ differ by no more than $\min\{M\xi, \lambda_0/AN\}$. What contributes to the image is the Fourier harmonic of such sources shifted by $\delta\omega = By$ with respect to the central frequency ω_0, cf. Eq. (6.4). The spread of y across the pinhole results into the spread of $|\delta\omega| \lesssim B(D_s - \delta y)$. If $M\xi \ll \lambda_0/AN$, then $D_s - \delta y = M_2 D - M\xi$ plays the role of the effective pinhole diameter in this measurement. The resultant formula for visibility, Eq. (6.19), is therefore similar to the Fraunhofer formula for diffraction through a slit of this *effective* width.

We compared experimental $V(\delta l)$ with the above theory treating ξ and M_2 as adjustable parameters. Instead of using the approximate Eq. (6.19), we evaluated Eq. (6.18) numerically. In agreement with Eq. (6.19) V was found to be most sensitive to ξ for Δ not too close to either zero or unity. It also happened that ξ was of the same order of magnitude as λ_0/ANM, and so the conditions for its estimation were nearly optimal.

As seen in Fig. 6.2d,e, there is a good agreement between the theory and the experiment. The measured $V(T)$, Fig. 3c, and the calculated $V(\xi)$, Fig. 6.3d, allow us to obtain the coherence length $\xi(T)$. Fig. 6.3e shows that the coherence length increases sharply at T below a few Kelvin. Intriguingly, the increase of ξ is in concert with the MOES formation.

Naively, the interference pattern of an extended source of length ξ washes out when $\xi\delta k \sim \pi$, where δk is a spread of the momentum distribution. For $\xi \sim 3\,\mu$m (Fig. 3e), this gives $\delta k \sim 10^4$ cm^{-1}, which is much smaller than the spread of the exciton momentum distribution in a classical exciton gas $\delta k_{cl} \sim \hbar^{-1}\sqrt{2mk_BT} \approx 3\times 10^5$ cm^{-1} at $T = 2$ K. In turn, this corresponds to a spread of the exciton energy distribution $\hbar^2\delta k^2/2m \sim 1\,\mu$eV, which is much smaller than that for a classical exciton gas $\delta E_{cl} \sim k_BT \approx 200\,\mu$eV at $T = 2$ K. It may also be interesting to estimate the exciton phase-breaking time $\tau_\phi = \xi^2/D_x$, where $D_x \sim 10\,\mathrm{cm}^2/\mathrm{s}$ [38] is the exciton diffusion coefficient. Using again $\xi = 3\,\mu$m, we get τ_ϕ of a few ns. In comparison, the inverse linewidth $\tau_c \approx 1\,$ps.

Let us now discuss physical mechanisms that may limit ξ and τ_ϕ. Since $\tau_{rec} \sim 40\,\mathrm{ns} \gg \tau_\phi$, the effect of exciton recombination on the phase-breaking time is negligible. Next, the excitons are highly mobile, as evidenced by their large diffusion length, ca. 30μm [50]; therefore, ξ is not limited by disorder localization. The coherence length may also be limited by inelastic collisions of excitons with phonons and with each other. For the high exciton densities $n \sim 10^{10}\,\mathrm{cm}^{-2}$ in our experiments, the dominant ones are the latter [36]. Note also that spontaneous coherence

we report arises in a cold thermalized exciton gas (the lifetime τ_{rec} of the indirect excitons is much longer than their thermalization time to $T = 2\,\mathrm{K}$, ~ 1 ns [12]), and is therefore different from the laser-like coherence in nonequilibrium systems due to a macroscopic coherent optical field [52].

Theoretical calculation of ξ due to exciton interactions is yet unavailable. It is expected however that inelastic processes should vanish at $T = 0$. Our findings call for developing a quantitative theory of phase-breaking processes in nonclassical exciton gases at low temperatures when the thermal de Broglie wavelength is comparable to the interparticle separation. In view of the exciting phenomena uncovered in both fermionic [4] and bosonic [5, 9, 22] systems at low temperatures, one can expect that rich physics may follow.

6.3 Spatial resolution effect

In this section we refine the model in previous section, and include the spatial resolution effect due to the limitation of collection optics in experiment.

Spatial coherence of a bosonic system is encoded in its one-body density matrix

$$\rho(\mathbf{r}) = \langle \Psi^\dagger(\mathbf{r}')\Psi(\mathbf{r}'+\mathbf{r})\rangle\,, \tag{6.9}$$

where $\Psi^\dagger$ (Ψ) is the particle creation (annihilation) operator and the averaging is over both the quantum state and the position $\mathbf{r}'$. In an isotropic system $\rho(\mathbf{r})$ depends on the absolute distance $r = |\mathbf{r}|$ only. The density matrix decreases with r as a result of scrambling the phases of the particles' wavefunctions by scattering and thermal fluctuations. When this decrease is faster than $1/r^2$, we can define a characteristic decay length of $\rho(r)$ — the coherence length — by the relation

$$\xi_x = \left(\int_0^\infty \rho(r) r dr\right) \Big/ \left(\int_0^\infty \rho(r) dr\right)\,. \tag{6.10}$$

Coherence length ξ_x provides a quantitative information about fundamental properties of the system of interest. For example, a rapid growth of ξ_x is anticipated as the bosons are cooled down below the temperature of their quantum degeneracy. [64, 40] In addition, ξ_x sheds light on interactions and disorder in the system.

Traditionally, real-space measurements of the optical coherence are done by two-slit (or two-point) interferometry. However, this method becomes inaccurate when ξ_x is smaller than the spatial width of the regions from which the light is collected. This is the case in our experiment where ξ_x does not exceed a few microns. However, our technique circumvents this limitation by using a single pinhole. It works well in the regime $\xi_x < D/M_1$, where D is the pinhole diameter and M_1 is the image magnification factor. In other words, the smallest measurable ξ_x is determined not by D/M_1 but by the finite spatial resolution of the optical system. In this part we show how this resolution can be taken into account.

In previous section we used an approximation of geometrical optics for describing the light collection in the apparatus. This is justified in the most interesting regime of low T where ξ_x is large. On the other hand, at the upper end of the temperature range shown in Fig. 6.3 the estimated coherence length ξ_x was comparable to the diffraction-limited resolution of the optical system, e.g., the Abbe limit [1, 44]

$$\mathrm{Ab} = \frac{\lambda_0}{2\,\mathrm{NA}}\,. \tag{6.11}$$

Here $\mathrm{NA} = \sin\alpha$ is the numerical aperture and λ_0 is the wavelength. In our experiment, $\mathrm{NA} = \sin 16^\circ \approx 0.3$ and $\lambda_0 \approx 800\,\mathrm{nm}$.

In this section we take diffraction into account and obtain refined estimates of ξ_x, which are shown in Fig. 6.4 by the triangles. The difference between previous and current estimates is insignificant for all but a few data points at the boundary of the experimental resolution. Therefore, the case for a rapid and strong onset of the spontaneous coherence of the exciton gas below the temperature of a few degrees K remains intact.

6.3.1 Relation between exciton and optical coherence lengths

It is well understood that the Abbe limit is not a "hard" limit but simply a characteristic measure of the optical resolution. In fact, another commonly used formulas due to Rayleigh [67, 8] differ from Eq. (6.11) by numerical factors. Roughly speaking, our theoretical model enables us to determine which numerical factor is appropriate for our method of measuring ξ_x. More precisely, our main result is as follows. Under certain assumptions, ξ_x is related to the *optical* coherence length ξ by

$$\xi = \sqrt{\xi_x^2 + \frac{1}{Q^2}} \ , \quad \frac{1}{Q} = \frac{\lambda_0}{2\pi \mathrm{NA}} \, . \tag{6.12}$$

Here, in analogy to Eq. (6.10), ξ is defined by

$$\xi = \frac{1}{M} \left(\int_0^\infty g(0,R) R dR \right) \Big/ \left(\int_0^\infty g(0,R) dR \right) \ , \tag{6.13}$$

where

$$g(t,R) = \langle E(t'+t, \mathbf{R}'+\mathbf{R}) E(t', \mathbf{R}') \rangle / \langle E^2(t', \mathbf{R}') \rangle \tag{6.14}$$

is the coherence function [8] of the PL signal $E(t, \mathbf{R})$ emitted by excitons and collected by the described system. In writing this formula we assumed, for convenience, that the second magnification (M_2) of the image occurs before the MZ interferometer, in which case $\mathbf{R}$ and $R = |\mathbf{R}|$ are, respectively, the two-dimensional and the radial coordinates in the plane of the fully magnified image.

Equation (6.12) is natural because an experimental measurement of any length is affected by the spatial resolution limit. However, Eq. (6.12) specifically indicates that for ξ_x measured using the setup depicted in Fig. 6.4a, the Abbe limit must be divided by π. This makes its effect quantitatively smaller than one would naively think.

In addition to the limitation from below, $\xi_x \gtrsim 1/Q$, the accuracy of the present method is restricted from above. When the coherence length exceeds the size of the

studied region of the sample D/M_1, the dependence of V on ξ_x should saturate, see the inset of Fig. 6.5. This may become important at low enough temperatures. The two limitations are indicated by the dashed lines in Fig. 6.4.

6.3.2 Geometrical optics approach

In order to construct the model of the described above measurement scheme, we need to know the functional form of $\rho(r)$. Unfortunately, at present there is no comprehensive theoretical framework that provides that. This is because $\rho(r)$ is affected by many factors, including thermal broadening and a variety of scattering mechanisms. On the other hand, the present state of experiment [81] does not allow us to extract reliably anything more than a characteristic decay length of function $\rho(r)$. Therefore, we take a phenomenological approach and consider two simple approximations for $\rho(r)$. The first one, used in Ref. [81], is an exponential

$$\rho(r) = \rho(0) \exp\left(-\frac{r}{\xi_x}\right) . \tag{6.15}$$

This *ansatz* should be reasonable over at least some range of r determined by the interplay of the disorder-limited mean-free path ($\sim 1\,\mu$m in high-mobility GaAs structures), thermal wavelength $\lambda_{\mathrm{dB}} \sim 0.1\,\mu$m, and possibly, some others. Most importantly, Eq. (6.15) provides a convenient starting point because it contains a single characteristic length ξ_x. Later in Sec. 6.3.3 we will also consider a Gaussian form,

$$\rho(r) = \rho(0) \exp\left(-\frac{r^2}{\pi\xi_x^2}\right) , \tag{6.16}$$

for comparison.

The crucial point is the relation between $\rho(r)$ and $g(R)$. (Here and below we drop t in the argument of g because the time-dependence is not relevant for the calculation.) If the experimental apparatus can be described by geometrical optics, then the only difference between the two functions is the linear magnification M and

rescaling by a constant factor. In this case, Eq. (6.15) entails

$$g(R) = g(0)\exp\left(-R/\,M\xi_x\right)\,. \tag{6.17}$$

In turn, Eq. (6.13) gives $\xi = \xi_x$, as expected. Until the very end of this section we will use these two lengths interchangeably.

We have shown previously [81] that the interference visibility contrast V is related to g as follows:

$$\begin{gathered} V = \theta(1-\Delta)V_0\,, \\ V_0 = \frac{\displaystyle\int_0^1 \frac{dz}{z}\sin[F(1-\Delta)z]\sin[F\Delta(1-z)]g(zD_s)}{\displaystyle F\Delta\int_0^1 \frac{dz}{z}\sin(Fz)(1-z)g(zD_s)}\,, \\ F = \pi\frac{AND_s}{\lambda_0}, \quad D_s = M_2 D, \quad \Delta = \frac{\delta l}{N\lambda_0}\,, \end{gathered} \tag{6.18}$$

where $\theta(z)$ is the step-function, A is the linear dispersion of the spectrometer, and N is the number of grooves in the diffraction grating. ($A = 1.55\,\mathrm{nm/mm}$ and $N = 1.5\times10^4$ in Ref. [81].)

For $g(r)$ given by Eq. (6.17) it is straightforward to compute the integrals in Eq. (6.18); however, in general it has to be done numerically. For short coherence lengths, $\xi \ll \lambda_0/\,ANM, D_s/M$, one can also derive the analytical formula [81]

$$V \simeq \left(1-\frac{\delta l}{N\lambda_0}\right)\left|\frac{\sin\pi X}{\pi X}\right|\,, \tag{6.19}$$

where

$$X = \frac{\delta l}{\delta l_0}\left(1-\frac{M}{D_s}\,\xi\right)\,, \quad \delta l_0 = \frac{\lambda_0^2}{AD_s}\,. \tag{6.20}$$

This equation can be obtained by expanding the sin-factors in the integrals to the order $\mathcal{O}(z)$ and extending their integration limits to infinity.

At $\delta l = \delta l_0$ and for small enough ξ, Eq. (6.19) yields

$$V(\delta l_0, \xi) \simeq \left(1 - \frac{\lambda_0}{AND_s}\right) \frac{M}{D_s}\, \xi\,. \tag{6.21}$$

Thus, as such δl the visibility contrast V vanishes unless ξ is nonzero. Working with $\delta l \approx \delta l_0$ ensures the highest sensitivity to ξ. In our experiment, [81] we extracted ξ at $\delta l = 4.2\,\mathrm{mm}$, which is close but not exactly equal to $\delta l_0 = 5.2\,\mathrm{mm}$. Therefore, we computed V using the full formula (6.18). The results are shown by the dashed line in Fig. 6.5. We fitted this theoretical curve $V(\xi)$ to the experimentally measured $V(T)$ (Fig. 6.3c) using $\xi = \xi(T)$ as an adjustable parameter. In this manner we obtain the graph shown by the squares in the main panel of Fig. 6.4. We see that the exciton coherence length exhibits a dramatic enhancement at $T < 4\,\mathrm{K}$. On the other hand, at $T \sim 4\,\mathrm{K}$ this approach gives $\xi_x = \xi \sim \lambda_0$. One can anticipate that the geometrical optics becomes inaccurate at such small ξ, so that ξ and ξ_x are in fact different. This question is studied in the next section.

6.3.3 Diffraction effects

The conventional theory [8] of the image formation in optical instruments laid down by Abbe [1] in 1873 predicts that a point source imaged by a lens with a magnification M creates the diffraction spot

$$E(R) \propto \int\limits_{k<Q} \frac{d^2k}{(2\pi)^2} e^{i\mathbf{kR}/M} = \frac{2MQ}{R}\, J_1\!\left(\frac{QR}{M}\right) \tag{6.22}$$

in the image plane. Here R is the radial distance, Q is given by Eq. (6.12), and $J_1(z)$ is the Bessel function. The field distribution (6.22) is known as the Airy diffraction pattern. [3] The physical meaning of Q is the largest tangential wavenumber admitted by the lens. Accordingly, the diffraction can be alternatively viewed as a low-pass filtering of the incoming light by the lens. [44]

The Airy pattern plays the role of the response function of the lens. Its finite spread in R imposes the limit on the achievable optical resolution $\sim Q^{-1}$ and is the source of the difference between the optical and the actual exciton coherence lengths, see Eq. (6.12). Indeed, because of the diffraction, the coherence function $g(R)$ is not just a rescaled copy of $\rho(R/M)$ but its convolution with the Airy pattern. Using tilde to denote the 2D Fourier transform, we can express this fact as follows:

$$\tilde{g}(k) \propto \theta(Q - Mk)\tilde{\rho}(Mk)\,. \tag{6.23}$$

Note that $\tilde{\rho}(k)$ has the physical meaning of the momentum distribution function for excitons. Computing $\tilde{\rho}(k)$ from Eq. (6.15), we get

$$\tilde{g}(k) = \text{const} \times \frac{\theta(Q - Mk)}{(1 + M^2\xi_x^2 k^2)^{3/2}}\,. \tag{6.24}$$

The constant prefactor in this formula has no effect on V. It is convenient to choose it to be $2\pi M^2\xi_x^2$, so that

$$g(R) = M^2\xi_x^2 \int_0^{Q/M} \frac{J_0(kR)kdk}{(1 + M^2\xi_x^2 k^2)^{3/2}}\,. \tag{6.25}$$

In this case in the limit $Q \to \infty$, we recover Eq. (6.17) with $g(0) = 1$. On the other hand, for finite Q, we have

$$g(0) = 1 - \frac{1}{\sqrt{1 + Q^2\xi_x^2}}\,. \tag{6.26}$$

Additionally, at large R, function $g(R)$ acquires the behavior characteristic of the Airy pattern (6.22): quasiperiodic oscillations with the envelope decaying as $R^{-3/2}$, see Fig. 6.6. Finally, computing the optical coherence length ξ according to Eq. (6.13) we get Eq. (6.12).

The refined theoretical dependence of V on ξ_x can now be obtained by substituting Eq. (6.25) into Eq. (6.18). As before, for small ξ_x analytical formulas (6.19)–(6.21)

suffice, with ξ defined by Eq. (6.12). When this ξ becomes comparable to D_s/M, numerical evaluation of Eqs. (6.18) and (6.25) is necessary. The representative results are shown by the solid line in Fig. 6.5. For comparison, two other curves are included. The dashed line is the geometrical optics approximation, $\xi = \xi_x$ of Subsec. 6.3.2. The dotted line is the result of correcting the latter according to Eq. (6.12) and using Q appropriate for our experiment. As one can see, at small ξ_x, the effect of the diffraction-limited resolution of the optical system is indeed accounted for by Eq. (6.12). At large ξ_x, the correction becomes small and all the curves are very close to each other.

It is instructive to examine how our conclusions so far depend on the model assumption (6.15) about function $\rho(r)$. To this end we consider next the Gaussian *ansatz* (6.16), which is similar to Maxwell-Boltzmann distribution except the coefficient in the exponential factor is adjusted to satisfy Eq. (6.10). Let us compute the corresponding ξ. Using Eq. (6.23), we can rewrite Eq. (6.13) as

$$\xi = \tilde{\rho}(0) \Big/ \left(\int_0^Q dk \tilde{\rho}(k) \right) . \tag{6.27}$$

Substituting here

$$\tilde{\rho}(k) = \tilde{\rho}(0) \exp\left(-\frac{\pi}{4} k^2 \xi_x^2 \right) , \tag{6.28}$$

which follows from Eq. (6.16), we get

$$\xi = \frac{\xi_x}{\operatorname{erf}\left[(\sqrt{\pi}/2) Q \xi_x \right]} , \tag{6.29}$$

where $\operatorname{erf}(z)$ is the error function. This formula replaces Eq. (6.12). Interestingly, it implies that for the same ξ_x and Q, the effect of the finite resolution in the case of a Gaussian decay is always smaller than for the exponential one. The direct numerical evaluation of Eq. (6.18) with the Gaussian profile (6.16) confirms this expectation, see Fig. 6.7. Thus, we again conclude that the diffraction correction is important for $\xi \lesssim \lambda_0$, but it is very small in the most interesting region $\xi > \lambda_0$.

Notice that function $V(\xi_x)$ increases somewhat faster with ξ_x for the Gaussian case compared to the exponential one, cf. Figs. 6.5 *vs.* 6.7. Therefore, had we adopted the Gaussian *ansatz* (6.16), the deduced values of $\xi_x(T)$ would have been somewhat smaller than those plotted in Fig. 6.4. This is to be expected: if the exact functional form of $\rho(r)$ is unknown, its characteristic decay length can be determined only up to a numerical coefficient of the order of unity.

6.3.4 Discussion

The main purpose of the present work is refinement of the optical method for determining the exciton coherence length ξ_x. Unlike previously proposed schemes, [41, 90] which involve angle-resolved photoluminescence, our technique is based on real-space interferometry.

We showed that in order to obtain an accurate estimate of ξ_x, the optical coherence length ξ of the exciton emission should be corrected because of the diffraction-limited spatial resolution of the experimental apparatus. However the correction is insignificant as long as ξ_x is larger than about one wavelength and the numerical aperture NA of the experimental setup is not too small. The correction does grow as NA decreases, and so reduced NA should be avoided.

It is well known [1, 44, 8] that limitation of the spatial resolution due to diffraction is equivalent to that due to restriction on tangential wavenumbers k admitted by the lens collecting the signal. This k-filtering effect has been considered in Ref. [59] in application to the measurements of the exciton coherence length. For the collection angle $\alpha = 16^\circ$ in our experiments, [81] the results presented in Fig. 3c of Ref. [59] give the correlation length due to the k-filtering effect $\xi_\gamma \approx 1\,\mu$m. (This length plays the role similar to that of $Q^{-1} = 0.42\,\mu$m in our formalism.) For the considered $\rho(r)$ this correction enters either through the quadratic sum, Eq. (6.12), or the error function, Eq. (6.29). As a result, the estimation of the k-filtering effect per Ref. [59]

gives only a small ($\sim 10\%$) correction, e.g., $\xi - \sqrt{\xi^2 - \xi_\gamma^2}$ to the optical coherence length ξ measured in Ref. [81] at low T. Therefore, it cannot explain the observed large enhancement of the coherence length at $T < 4\,\mathrm{K}$. Our calculations indicate that the correction is even smaller.

The discussion of physics that is responsible for the observed rapid change in ξ_x at low temperatures is however beyond the score of this thesis. As a final word, we would like to offer only the following minimal remarks on this matter.

The density matrix $\rho(r)$, from which ξ_x is defined through Eq. (6.10), is influenced by a number of factors, including Bose statistics, interactions, and scattering. The effect of the first two has been studied extensively, albeit for simplified models of interaction. According to present understanding, [64, 40] the long-distance behavior of function $\rho(r)$ is qualitatively different above and below the Berezinskii-Kosterlitz-Thouless (BKT) transition temperature T_{BKT}. At $T \gg T_{\mathrm{BKT}}$, where $\tilde{\rho}(k)$ obeys the classical Boltzmann statistics, $\rho(r)$ decays as a Gaussian, Eq. (6.16), with the coherence length

$$\xi_x = \lambda_{\mathrm{dB}}/\pi\,. \tag{6.30}$$

[Our estimates of ξ_x at $T < 4\,\mathrm{K}$ exceed $\lambda_{\mathrm{dB}}/\pi$ by an order of magnitude, suggesting that Eq. (6.30) does not apply at such temperatures.] At $T < T_{\mathrm{BKT}}$, the eventual asymptotic decay of the density matrix becomes algebraic, $\rho(r) \propto r^{-\nu}$ with a temperature-dependent exponent $\nu(T)$. The behavior of $\rho(r)$ at intermediate temperatures and/or distances is more complicated. In general, it can be computed only numerically, e.g., by quantum Monte-Carlo method. [40]

Some of the other mechanisms of limiting the coherence length ξ_x, such as exciton recombination and exciton-phonon scattering are too weak to significantly affect the large magnitude of observed ξ_x at low temperatures. [81] However, scattering by impurities and defects should be seriously considered. It can substantially modify the functional form of $\rho(r)$ compared to the disorder-free case. Indeed, weak disorder typically leads to an exponential decay of the correlation functions on the scale of

the mean-free path, which in fact inspired our *ansatz* (6.15). As temperature goes down, the strength of the disorder decreases because excitons can screen it more efficiently. [11, 60, 37] This should increase both the mean-free path and the exciton coherence length.

The comprehensive theoretical calculation of the exciton coherence length that would take into account all relevant thermal, interaction, and disorder screening effects is yet unavailable.

6.4 Another way to measure spatial coherence

Another way of measuring spatial coherence is to use two pinholes instead of one. Fig. 6.8a shows the experimental setup. In each arm of the MZ interferometer, there is a pinhole ($D = 10\mu m$) to select PL from one spot of the sample. The two spots separate by distance δx on the sample. The magnification factor from sample to pinhole is $M_1 = 5$. So the size of pinhole on the sample is $D/M_1 = 2\mu m$ (Fig. 6.8c).

We use the same sample and the same He-Ne laser in this experiment. The laser were patterned into a laser excitation ring with a diameter of 30 μm and a ring thickness following a Gaussian profile of FWHM = 10 μm using a shadow mask. This ring shape excitation creates an optical trap for exciton [32]. The pinholes selected PL from exciton cloud in the center of this optical trap . We still use the same spectrometer with the same grating and CCD to collect signal. We observed the similar interference fringe as in single pinhole experiment. Fig. 6.8b shows the interference contrast versus δx for different temperatures, $T = 1.6K$ (black) and $T = 8K$ (red).

Let us proceed to data processing. The photon can be written as $E(r, t)$. After MZ interferometer, the photon from both arms will be $E(r1, t1)+E(r2, t2)$, here path length difference between the two arms in MZ interferometer is the same as previous experiment $\delta l = 4.2mm$, so $t1 - t2 = 14ps$, and $r1 - r2 = \delta x$. The interference

contrast will be just $< E(r+\delta x, t+14ps)E(r,t) > / < E^2(r,t) >= g(14ps, \delta x)$. From the ansatz $g(t, \mathbf{r}) = g(t,0)\exp(-r/\xi)$, the contrast is just $g(14ps, 0)\exp(-r/\xi)$. Thus contrast of the interference fringe is spatial coherence function. From Fig. 6.8b, we can directly get exciton spatial coherence length ξ.

From data in 8K, we get $\xi = 1.5\mu m$. This is indeed just out spatial resolution. The objective we used has a $N.A. = 0.28$. The PL wavelength is around 800nm, so $R = 0.61 \times \lambda/N.A. = 1.75\mu m$. This is also proved our system is well aligned. Because if pinholes are not in the same image plane as the sample, the coherence length we measured ξ will be longer.

In low temperature, $T = 1.6K$, we can see the coherence length increased, $\xi = 3\mu m$, same as one-pinhole measurement.The exciton density in the center of optical trap is around $10^{10} cm^{-2}$, similar as the density of exciton in center of MOES. So the results from two different ways of measurement agree with each other.

But two-pinhole way is greatly limited by the spatial resolution of objective, so it is not accurate for small ξ, while the maximum spatial coherence measured in one-pinhole experiment is limited by the size of pinhole. So one-pinhole measurement is good when coherence length is small, while two-pinhole measurement is good when coherence length is large.

Also, we can confirm the one pinhole results from fig. 6.8b. When $\delta x = 0$, the setup becomes one-pinhole experiment. There is a small drop off in interference contrast from low temperature to high temperature. This is in agreement with results in Fig. 6.2d.

6.5 Acknowledgements

The text of chapter 6, in part, is a reprint of the material as it appears in Sen Yang, A.T. Hammack, M.M. Fogler, L.V. Butov, and A.C. Gossard, *Coherence Length of Cold Exciton Gases in Coupled Quantum Wells*, Phys. Rev. Lett. **97**, 187402,

The text of chapter 6, in part, is a reprint of the material as it appears in M.M. Fogler, Sen Yang, A.T. Hammack, L.V. Butov, and A.C. Gossard, *Effect of spatial resolution on the estimates of the coherence length of excitons in quantum wells*, Phys. Rev. B **78**, 035411,

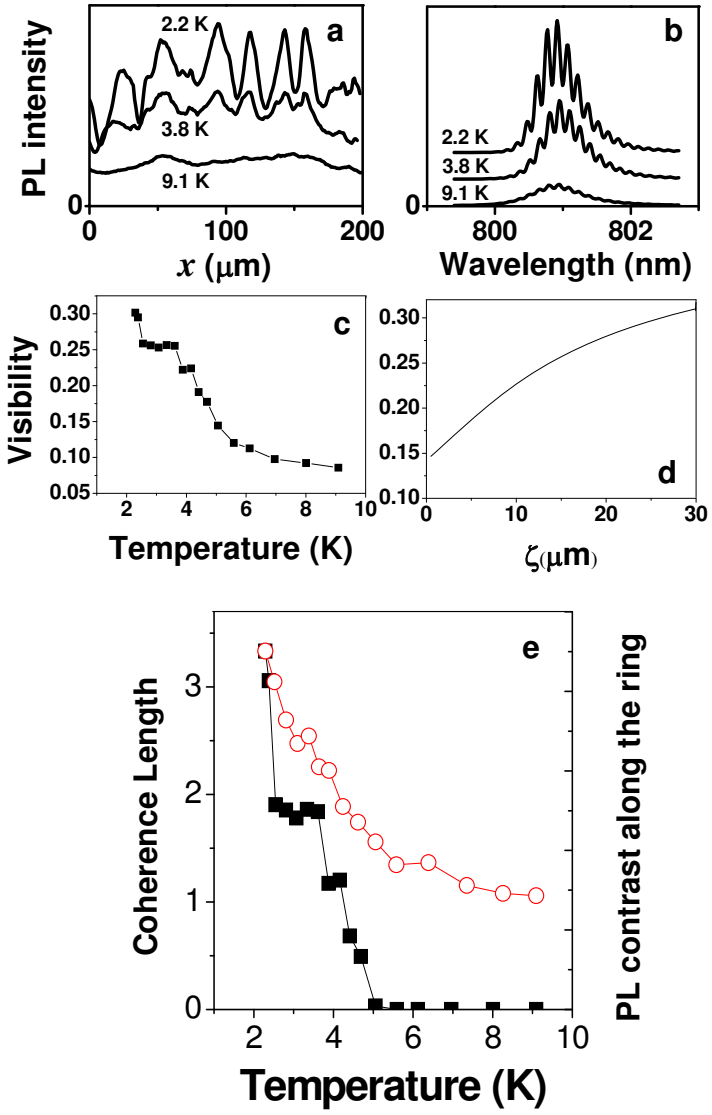

Figure 6.3: (a) Variations of the indirect exciton PL intensity along the external ring at $T = 2.2, 3.8$, and 9.1 K. (b) Interference profiles at $T = 2.2, 3.8$, and 9.1 K for $D = 50\,\mu$m and $\delta l = 4.2$ mm. (c) Visibility of the interference fringes vs T. (d) Calculated visibility as a function of the coherence length for $M_2 = 1.7$. (e) The exciton coherence length (squares) and contrast of the spatial intensity modulation along the ring (circles) vs T. The shaded area is beyond experimental accuracy. $V_g = 1.24\,$V, $P_{ex} = 0.7$ mW for all the data; $D = 50\,\mu$m, and $\delta l = 4.2$ mm for the data in (b)-(e). [81]

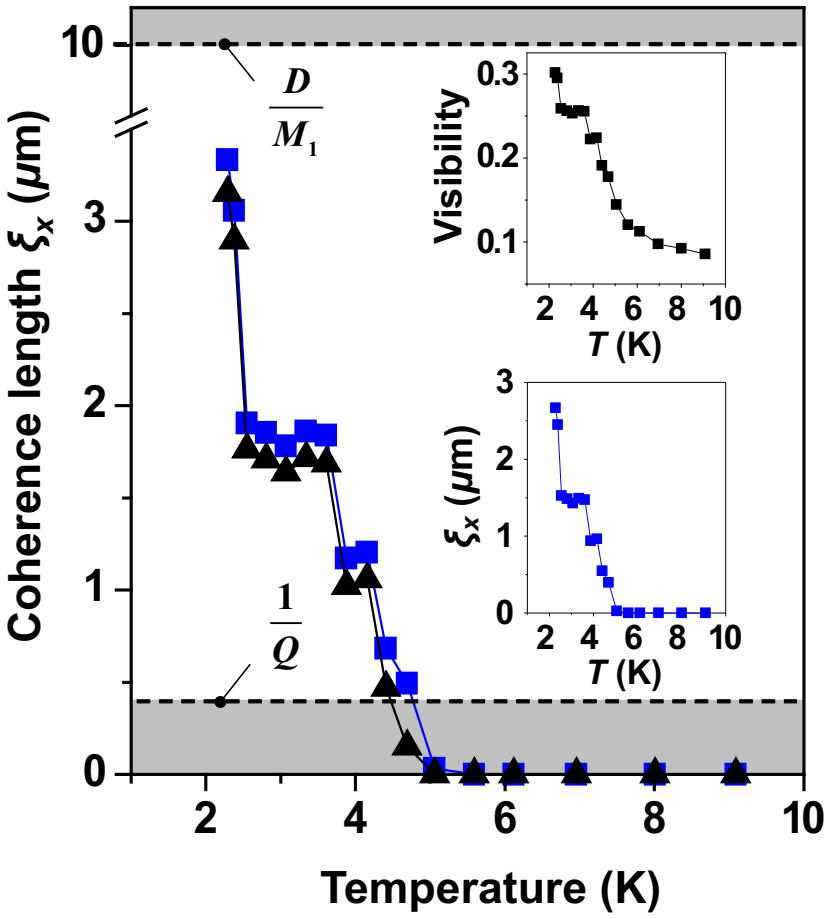

Figure 6.4: Main panel: ξ_x deduced from the fits of $V(T)$ to the theoretical curves in Fig. 6.5. The triangles (squares) are the estimates with (without) taking into account the spatial resolution of the experimental setup. The dashed lines indicate boundaries of experimental accuracy. Inset: previous estimates of the coherence length. [26]

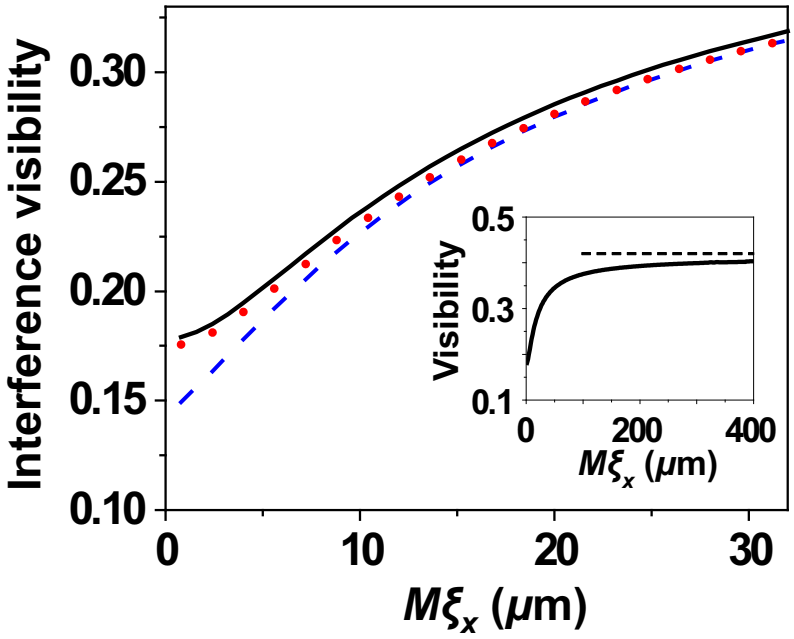

Figure 6.5: Visibility of the interference fringes *vs.* ξ_x for parameters $\delta l = 4.2\,\mathrm{mm}$, $D = 50\,\mu\mathrm{m}$, $M_1 = 5$, $M_2 = 1.6$, $Q^{-1} = 0.42\,\mu\mathrm{m}$. The solid line is the current theory; the dashed line is from Ref. [81]; the dotted line is obtained from the dashed one by the replacement $\xi_x \to \sqrt{\xi_x^2 + Q^{-2}}$. The inset shows function $V(\xi_x)$ over a larger range of ξ_x, with the dashed line indicating the asymptotic value $V(\xi_x = \infty)$. [26]

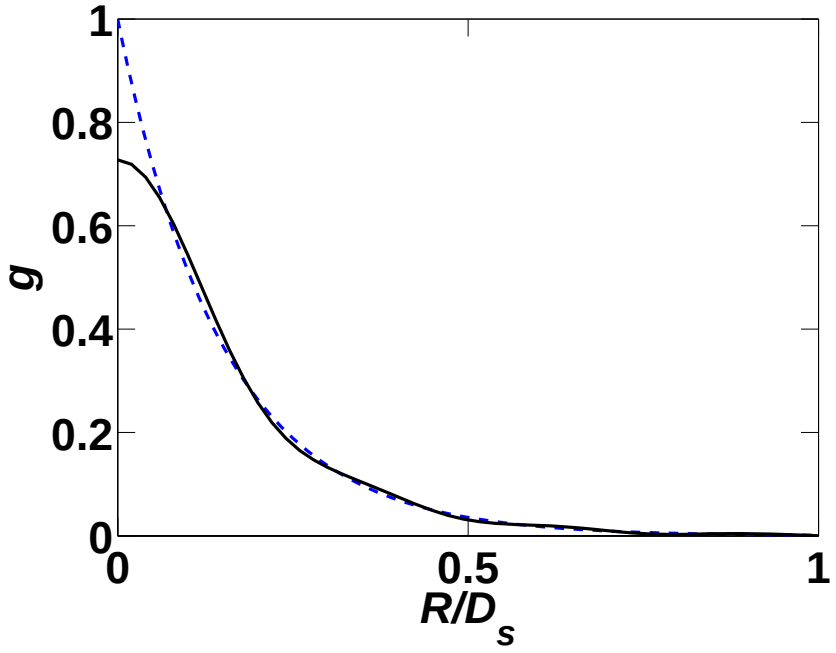

Figure 6.6: Optical coherence function $g = g(R)$. The solid line is computed for the following set of parameters: $\xi_x = 1.5\,\mu$m, $M = 8$, $Q^{-1} = 0.42\,\mu$m, and $D_s = 80\,\mu$m. The dashed line is for geometrical optics, $Q^{-1} = 0$. [26]

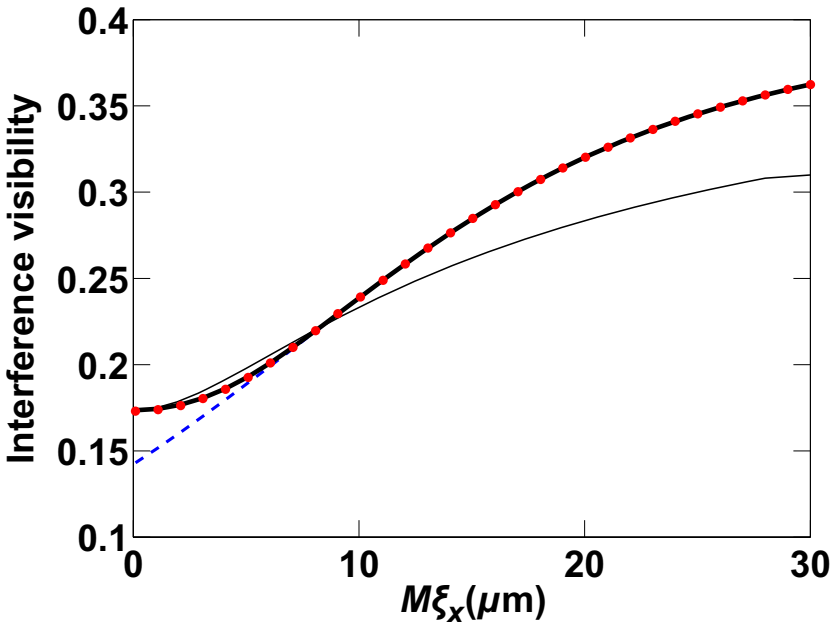

Figure 6.7: Visibility of the interference fringes *vs.* ξ_x for the Gaussian coherence function (6.16) and the parameters of Fig. 6.5. The thick solid line includes the diffraction correction; the dashed line is for the geometrical optics; the dotted line is obtained from the dashed one by the replacement of ξ_x by ξ according to Eq. (6.29). The thin solid line is $V(\xi_x)$ for the exponential *ansatz*, replotted from Fig. 6.5 to facilitate the comparison. [26]

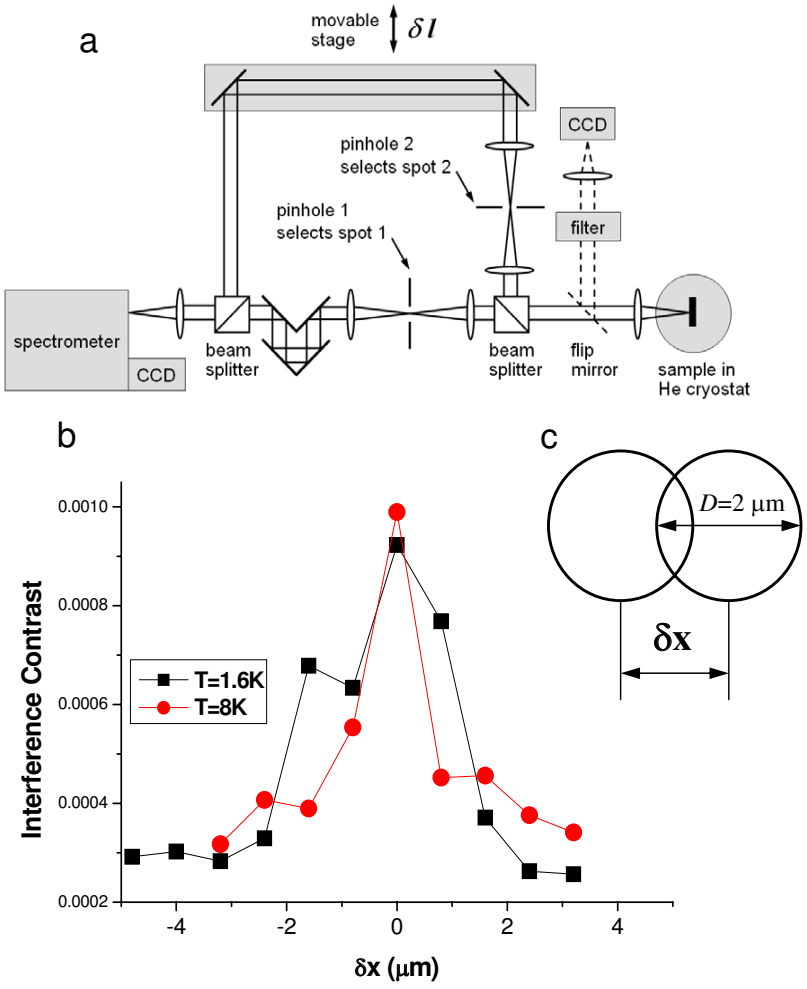

Figure 6.8: (a) scheme of MZ interferometer with a pinhole in each arm and with spatial and spectral resolution. (b) Visibility of the interference fringes vs δx for two temperatures: 1.6K (black) and 8K(red). (c) scheme of the relative pinhole position.

Chapter 7

Summary and Future Work

7.1 Summary

In this thesis, we presented the optical studies of indirect exciton in coupled quantum wells. Several features of PL patterns have been studied, including inner exciton rings , the external exciton rings , the localized bright spots(LBS). We performed the first time-resolved and spatial resolved kinetics measurements for the pattern formation. Simulation based on in-plane charge separation model gave good agreement with experiment. Diffusion constant of electrons and holes are obtained from the simulation fit.

Indirect exciton has long lifetime, fast cooling speed, so it can be cooled to low temperature. The exciton temperature we realized in experiment is below de Broglie temperature when exciton gas becomes quantum. At this temperature, we observed the macroscopically ordered exciton state (MOES) in external ring. This MOES state is a low temperature state, the transition temperature is near de Broglie temperature. By measuring the energy and density profile along the external ring, we determined interaction between excitons in this system is repulsion, so attraction cannot be the origin of this state. Commensurability was observed in this density wave. When

there is integer number of wavelength between two LBS, the density wave is stable. The model based on stimulated scattering agrees with experimental results.

Spatial coherence was measured by two different ways in this cold exciton gas. A strong enhancement of the exciton coherence length was observed at temperatures below a few Kelvin. The increase of the coherence length is correlated with the macroscopic spatial ordering of excitons. The coherence length at the lowest temperature corresponds to a very narrow spread of the exciton momentum distribution, much smaller than that for a classical exciton gas.

7.2 Future work

There are several interesting questions need to be answered in those fields.

For pattern formation: one question is what the pattern will look like in magnetic field. Magnetic field will have several influence in pattern formation. When magnetic field is applied in z direction, exciton effective mass increases. A simple picture to look at this: exciton moves in B field, electron and hole are moving in cyclotron motion in opposite direction, so extra energy is used to pull electron and hole apart, so the mass increase. Therefore exciton tends to be localized in B field. External ring is made by transportation of both electrons and holes. In B field, both electron and hole will do cyclotron motion and localized. So the density of excitons in external ring will reduce.[17] All those effects should influence the formation of external ring and MOES state.

Another interesting program will be: pattern formation in a 1D trap. External ring is like a 1D tube, when excitons are in a 1D trap, pattern may form in exciton gas.

Further study in coherence:

In dilution fridge, the lattice temperature can go below 90mK, for exciton lifetime around 100ns, exciton cloud can be cooled down to 100mK, this is much lower than

critical temperature of BEC, majority of excitons should condense into the lowest state. So the time coherence and spatial coherence could be high. Also it will be interesting to study the change of linewidth at that condition.

Other ways of measuring coherence can be used. For example, we can image at the Fourier plane of objective. In this plane, spatial position corresponds to angular momentum, thus in-plane momentum of excitons. Speckles are expected in strong coherence case [48]. A theory [86] predicts spin-dependent circulation in trapped exciton gas and instability in an exciton condensate in favor of vortex formation. If vortex exists in the system, it may be observed in this momentum plane [45]. Also, transition from superfluidity to localized state can be observed in this plane. Finding Fourier plane is not hard in experiment. Because the back plane of the objective is just its Fourier plane.

There are others ways to probe spatial coherence. A modified Michelson interferometer was used in [39]. In one part of interferometer, a set of mirrors flips the image. After signals from both path overlap, interference fringes will show up if the spatial coherence is long enough.

In [24], two slits tilted an angle with each other are used as variable distance double pinholes. Interference fringes will be observed in far field if there is spatial coherence.

Magnetic field also changes condensation and coherence. There are several effects. The magnetic field increases the in-plane exciton mass M_X and, therefore, reduces the quantum degeneracy of the 2D exciton gas and T_c which are both $\propto 1/M_X$. On the other hand, magnetic field lifts off the spin degeneracy, g, resulting in an increase of the quantum degeneracy and of the exciton condensation critical temperature T_c which are both $\propto 1/g$. Another factor is: magnetic field makes a coupling between the exciton center of mass motion and internal structure. The electron hole attraction will force exciton stay in low momentum state, which is a benefit to generate condensation. The increasing of binding energy and reduction of radius will also

help condensation [17]. In AlAs/GaAs CQWs with d=3.5 nm, change of mass is not significant due to small separation d, the life of spin degeneracy plays the most important role, so with magnetic field, the quantum degeneracy improved [10, 11]. In GaAs/AlGaAs sample with d= 11.5 nm, change of mass is significant due to large separation d, magnetic field reduces the quantum degeneracy [12]. Coherence measurement has not been done in those conditions yet. Experiments of coherence should give us some insights.

Bibliography

[1] E. Abbe, Arch. f. Mikroskop. Anat. **9**, 413 (1873).

[2] J.R. Abo-Shaeer, C. Raman, J.M. Vogels, and W. Ketterle. Science **292**, 476 (2001).

[3] G. B. Airy, Phil. Mag. Ser. 3 **18**, 1 (1841). The Airy formula is actually not exact but it is a good approximation near the optical axis, see J. D. Jackson, *Classical Electrodynamics* (Wiley, New York, 1998).

[4] B.L. Altshuler, P.A. Lee, and R.A. Webb, *Mesoscopic Phenomena in Solids*, edited by V.M. Agranonich and A.A. Maradudin (North-Holland, Amsterdam 1991).

[5] M. H. Anderson, J. R. Ensher, M. R. Matthews, C. E. Wieman, E. A. Cornell, Science **269**, 198 (1995).

[6] M.R. Andrews,C.G. Townsend, H.J. Miesner, D.S. Durfee, D.M. Kurn and W. Ketterle, Science **275** 637(1997)

[7] D. Birkedal and J. Shah, Phys. Rev. Lett. **81**, 2372 (1998).

[8] M. Born and E. Wolf, *Principles of Optics*, 7th ed. (Cambridge University Press, Cambridge, UK, 1999).

[9] C. C. Bradley, C. A. Sackett, J. J. Tollett, R. G. Hulet, Phys. Rev. Lett. **75**, 1687 (1995).

[10] L. V. Butov, A. Zrenner, G. Abstreiter, G. Böhm, and G. Weimann, Phys. Rev. Lett. **73**, 304 (1994).

[11] L. V. Butov and A. I. Filin, Phys. Rev. B **58**, 1980 (1998).

[12] L.V. Butov, A.L. Ivanov, A. Imamoglu, P.B. Littlewood, A.A. Shashkin, V.T. Dolgopolov, K.L. Campman, and A.C. Gossard, Phys. Rev. Lett. **86**, 5608 (2001).

[13] L.V. Butov, A.C. Gossard, and D.S. Chemla, cond-mat/0204482; Nature **418**, 751 (2002).

[14] L.V. Butov, C.W. Lai, A.L. Ivanov, A.C. Gossard, D.S. Chemla, Nature **417**, 47 (2002).

[15] L.V. Butov, Solid State Commun. **127**, 89 (2003).

[16] L.V. Butov, L.S. Levitov, A.V. Mintsev, B.D. Simons, A.C. Gossard, D.S. Chemla, cond-mat/0308117; Phys. Rev. Lett. **92**, 117404 (2004).

[17] L.V. Butov, J. Phys.: Condens. Matter **16**, R1577 (2004).

[18] V. Castets, E. Dulos, J. Boissonade, and P. De Kepper Phys. Rev. Lett. 64, 29532956 (1990)

[19] S. Chandrasekhar, E. Fermi, Astrophys. J. **118**, 116 (1953).

[20] D.S. Chemla and J. Shah, Nature **411**, 549 (2001).

[21] Gang Chen, Ronen Rapaport, Steven H. Simon, Loren Pfeiffer, and Ken West, arXiv:cond-mat/0412272 (2004).

[22] K. B. Davis, M. O. Mewes, M. R. Andrews, N. J. Vandruten, D. S. Durfee, D. M. Kurn, W. Ketterle, Phys. Rev. Lett. **75**, 3969 (1995).

[23] M.M. Dignam and J.E. Sipe, Phys. Rev. B 43, 4084 (1991).

[24] F. Dubin, R. Melet, T. Barisien, R. Grousson, L. Legrand, M. Schott, and V. Voliotis, Nature Physics **2** 33 (2006).

[25] D. S. Fisher and P. C. Hohenberg, Phys. Rev. B **37**, 4936 (1988).

[26] M.M. Fogler, Sen Yang, A.T. Hammack, L.V. Butov, and A.C. Gossard, cond-mat/0804.2686 (2008). Phys. Rev. B **78**, 035411 (2008)

[27] J. Fortágh, H. Ott, S. Kraft, A. Günther, and C. Zimmermann. Phys. Rev. A **66**, 041604 (2002); A. E. Leanhardt, A. P. Chikkatur, D. Kielpinski, Y. Shin, T. L. Gustavson, W. Ketterle, and D. E. Pritchard. Phys. Rev. Lett. **89**, 040401 (2002)

[28] T. Fukuzawa, S. S. Kano, T. K. Gustafson, and T. Ogawa, Surf. Sci. **228**, 482 (1990).

[29] M. Greiner, O. Mandel, T. Esslinger, T. W. Haensch, and I. Bloch Nature **415** 39, 2002

[30] S. Haacke, S. Schaer, and B. Deveaud, V. Savona, Phys. Rev. B 61, R5109 (2000).

[31] M. Haque, Phys. Rev. E **73**, 066207 (2006)

[32] A.T. Hammack, M. Griswold, L.V. Butov, L.E. Smallwood, A.L. Ivanov, and A.C. Gossard, Phys. Rev. Lett. **96**, 227402 (2006).

[33] A.A. High, A.T. Hammack, L.V. Butov, L. Mouchliadis, A.L. Ivanov, M. Hanson, and A.C. Gossard, arXiv:0804.4886v1 (2008).

[34] P. Hohenberg. Physical Review **158**, 383 (1967).

[35] Kerson Huang, *Statistical Mechanics*, 2nd ed. (John Wiley and Sons, 1987).

[36] A.L. Ivanov, P.B. Littlewood, H. Haug, Phys. Rev. B **59**, 5032 (1999).

[37] A. L. Ivanov, Europhys. Lett. **59**, 586 (2002).

[38] A.L. Ivanov, L.E. Smallwood, A.T. Hammack, Sen Yang, L.V. Butov, and A.C. Gossard, Europhys. Lett. **73**, 920 (2006)

[39] J. Kasprzak, M. Richard, S. Kundermann, A. Baas, P. Jeambrun, J. M. J. Keeling, F. M. Marchetti, M. H. Szymanska, R. Andre, J. L. Staehli, V. Savona, P. B. Littlewood, B. Deveaud and Le Si Dang, Nature **443** 413 (2006).

[40] Yu. Kagan, V. A. Kashurnikov, A. V. Krasavin, N. V. Prokof'ev, and B. V. Svistunov, Phys. Rev. A **61**, 043608 (2000).

[41] J. Keeling, L. S. Levitov, and P. B. Littlewood, Phys. Rev. Lett. **92**, 176402 (2004).

[42] L.V. Keldysh, Yu.V. Kopaev, *Sov. Phys. Solid State* **6**, 2219 (1965).

[43] L.V. Keldysh, A.N. Kozlov, *Sov. Phys. JETP* **27**, 521 (1968).

[44] H. Köhler, J. Mod. Opt. **28**, 1691 (1981).

[45] K. G. Lagoudakis, M. Wouters, M. Richard, A. Baas, I. Carusotto, R. Andre, Le Si Dang and B. Deveaud-Pledran, Nature Physics **4** 706 (2008).

[46] C.W. Lai, J. Zoch, A.C. Gossard, D.S. Chemla, Science **303**, 503 (2004).

[47] B. Laikhtman, Europhys. Lett. **43**, 53 (1998).

[48] W. Langbein, J.M. Hvam, and R. Zimmermann, Phys. Rev. Lett. **82**, 1040 (1999).

[49] E.B. Jacob, I. Becker, Y. Shapira, and H. Levine, Trends in Microbiology **12**, 366 (2004).

[50] L.S. Levitov, B.D. Simons, and L.V. Butov, Phys. Rev. Lett. **94**, 176404 (2005).

[51] L.S. Levitov, B.D. Simons, and L.V. Butov, Solid State Commun. **134**, 51 (2005).

[52] For a review, see P.B. Littlewood, P.R. Eastham, J.M.J. Keeling, F.M. Marchetti, B.D. Simons, and M.H. Szymanska, J. Phys.: Condens. Matter **16**, S3597 (2004).

[53] R. Loudon, *The Quantum Theory of Light*, 3d ed. (Oxford University Press, 2000).

[54] Yu. E. Lozovik and V. I. Yudson, Pis'ma Zh. Eksp. Teor. Fiz. **22**, 556 (1975) [JETP Lett. **22**, 274 (1975)].

[55] Yu.E. Lozovik and O.L. Berman, JETP Lett. **64**, 573 (1996).

[56] Yu.E. Lozovik, I.V. Ovchinnikov, S.Yu. Volkov, L.V. Butov, and D.S. Chemla, Phys. Rev. B **65**, 235304 (2002).

[57] X. Marie, P.Le Jeune, T. Amand, M. Brousseau, J. Barrau, M. Paillard, R. Planel, Phys. Rev. Lett. **79**, 3222 (1997).

[58] M.-O. Mewes, M. R. Andrews, D. M. Kurn, D. S. Durfee, C. G. Townsend, and W. Ketterle, Phys. Rev. Lett. **78**, 582 (1997).

[59] L. Mouchliadis and A. L. Ivanov, Phys. Rev. B **78**, 033306 (2008).

[60] D. E. Nikonov and A. Imamoglu, arXiv:quant-ph/9806003.

[61] A. Olaya-Castro, F. J. Rodriguez, L. Quiroga, and C. Tejedor, Phys. Rev. Lett. **87**, 246403 (2001).

[62] Th. Östereich, T. Portengen, and L.J. Sham, Solid State Commun. **100**, 325 (1996).

[63] C.J. Pethick, H. Smith, *Bose-Einstein condensation in dilute gases*. (Cambridge University Press, 2002).

[64] V. N. Popov, Theor. Math. Phys. **11** 565 (1972).

[65] N. Prokof'ev and B. Svistunov, Phys. Rev. A **66**, 043608 (2002).

[66] R. Rapaport, G. Chen, D. Snoke, S.H. Simon, L. Pfeiffer, K. West, Y. Liu, S. Denev, cond-mat/0308150; Phys. Rev. Lett. **92**, 117405 (2004).

[67] L. Rayleigh, Mon. Notes Roy. Astron. Soc. **33** 59 (1872). Reprinted in L. Rayleigh, *Scientific Papers* (Dover, New York, 1964), Vol. I, p. 163.

[68] M. Remeika, J.C. Graves, A.T. Hammack, A.D. Meyertholen, M.M. Fogler, L.V. Butov, M. Hanson, A.C. Gossard, arXiv:0901.1349 (2009).

[69] C. Schindler and R. Zimmermann, Phys. Rev. B **78**, 045313 (2008).

[70] M.O. Scully and M.S. Zubairy, *Quantum Optics* (Cambridge University Press, 1997).

[71] J. Shah, *Ultrafast Spectroscopy of Semiconductors and Semiconductor Nanostructures*, 2nd Ed. (Springer, 1999)

[72] S. I. Shevchenko, Fiz. Nizk. Temp. **2**, 505 (1976) [Sov. J. Low Temp. Phys. **2**, 251 (1976)].

[73] D. Snoke, S. Denev, Y. Liu, L. Pfeiffer, K. West, Nature **418**, 754 (2002).

[74] K.E. Strecker, G.B. Partridge, A.G. Truscott, R.G. Hulet, Nature **417**, 150 (2002).

[75] V.I. Sugakov, Solid State Commun. **134**, 63 (2005).

[76] A.A. Chernyuk and V.I. Sugakov, Phys. Rev. B **74**, 085303 (2006).

[77] G.I. Taylor, Phil. Trans. R. Soc. A **223**, 289 (1923)

[78] E.B. Jacob, I. Becker, Y. Shapira, H. Levine, TRENDS in Microbiology **12**, 366 (2004).

[79] Daw-Wei Wang, Mikhail D. Lukin, and Eugene Demler. Phys. Rev. Lett. **92**, 076802 (2004)

[80] J. Yang, I. Makasyuk, P. G. Kevrekidis, H. Martin, B. A. Malomed, D. J. Frantzeskakis, and Zhigang Chen. Phys. Rev. Lett. **94**, 113902 (2005)

[81] S. Yang, A. T. Hammack, M. M. Fogler, L. V. Butov, and A. C. Gossard, Phys. Rev. Lett. **97**, 187402 (2006).

[82] S. Yang, A.V. Mintsev, A.T. Hammack, L.V. Butov, and A.C. Gossard, Phys. Rev. B **75**, 033311 (2007).

[83] S. Yang, L.S. Levitov, B.D. Simons, L.V. Butov, and A.C. Gossard, unpublished

[84] S. Yang, L.S. Levitov, B.D. Simons, L.V. Butov, and A.C. Gossard, unpublished

[85] S.-R.Eric Yang, Q-Han Park, and J. Yeo. Laser Physics **15**, 388 (2005)

[86] Wang Yao and Qian Niu, Phys. Rev. Lett. **101**, 106401 (2008)

[87] D. Yoshioka and A.H. MacDonald, J.Phys. Soc. Jpn. **59**, 4211 (1990).

[88] P.Y. Yu, M. Cardona, *Fundamentals of Semiconductors*, 3rd ed. (Springer, 2001)

[89] X. Zhu, P.B. Littlewood, M. Hybertsen, and T.M. Rice, Phys.Rev.Lett. **74**, 1633 (1995).

[90] R. Zimmermann, Solid State Commun. **134**, 43 (2005).